January 2013

Characterization Of Evaporative Metal Bonding In Superalloys For Use In Gasified Coal Turbine Generators

Joshua Elliot Braband

CHARACTERIZATION OF EVAPORATIVE METAL BONDING IN SUPERALLOYS FOR USE IN GASIFIED COAL TURBINE GENERATORS

by

Joshua Elliot Braband
Bachelor of Science, Minnesota State University Mankato, 2011

A Thesis

Submitted to the Graduate Faculty

of the

University of North Dakota

In partial fulfillment of the requirements

for the degree of

Master of Science

Grand Forks, North Dakota
August
2013

This thesis, submitted by Joshua Elliot Braband in partial fulfillment of the requirements for the Degree of Master of Science in Mechanical Engineering from the University of North Dakota, has been read by the Faculty Advisory Committee under whom the work has been done, and is hereby approved.

Matthew Cavalli, Ph.D., P.E.

William Semke Ph.D.

George Bibel, Ph.D., P.E.

This thesis is being submitted by the appointed advisory committee as having met all of the requirements of the Graduate School at the University of North Dakota and is hereby approved.

Dean of the Graduate School

July 29, 2013
Date

Title CHARACTERIZATION OF EVAPORATIVE METAL BONDING IN SUPERALLOYS FOR USE IN GASIFIED COAL TURBINE GENERATORS

Department Mechanical Engineering

Degree Masters of Science

In presenting this thesis in partial fulfillment of the requirements for a graduate degree from the University of North Dakota, I agree that the library of this University shall make it freely available for inspection. I further agree that permission for extensive copying for scholarly purposes may be granted by the professor who supervised my thesis work or, in his absence, by the Chairperson of the department or the Dean of the Graduate School. It is understood that any copying or publication or other use of this thesis or part thereof for financial gain shall not be allowed without my written permission. It is also understood that due recognition shall be given to me and to the University of North Dakota in any scholarly use which may be made of any material in my thesis

Joshua Elliot Braband
July 24, 2013

TABLE OF CONTENTS

LIST OF FIGURES vii

LIST OF TABLES x

ACKNOWLEDGMENTS xi

ABSTRACT xii

CHAPTER

I. INTRODUCTION

Project Purpose 1

Overview of Diffusion Bonding 2

Prior Work 6

Prior Work Overview 6

Bonding Pressure 7

Bonding Temperature 11

Finite Element Modeling 13

Current Work 18

II. METHODS

Overview 20

Material Selection 20

Bonding Alloys 20

Interlayer 22

Other Metals 22

Creation of Diffusion Bonded Samples 24

Finite Element Modeling 26

III. DATA AND ANALYSIS

Diffusion Data 33

Diffusion Data Analysis 42

Finite Element Model Data 45

Finite Element Model Data Analysis 57

IV. CONCLUSION

Summary 69

Results Summary 71

Future Work 73

Conclusion 74

APPENDIX 76

REFERENCES 91

LIST OF FIGURES

Figures Page

1. a) Voids Present During Initial Contact Between the Materials
b) Voids Present After the Clamping Force is Applied 3

2. Diagram of Interlayer Movement in Evaporative Metal Bonding 5

3. The Effect of Reduction Percent on Bonding Strength [15] 9

4. Hardness Distribution in a Diffusion Joint Before and After Heat
Treatment Across the Bondline [18] 12

5. Microstructure of Rene 80 a) As Bonded b) After Post Bonding Heat
Treatment [20] 13

6. a) Diagram of Diffusion Bonded Joint b) Distribution of Residual Stress
(in Pa) [32] 16

7. Hardness of Rene 80 Variation from Center of Bond [20] 17

8. a) Bonding Jig Fixture Geometry (units in cm) b) Assembled Bonding
Fixture 23

9. Pressure Film 28

10. a) Model Used for Simulation of CM247LC and Rene 80 Bonding
b) Model Used for Simulation of APMT Bonding 30

11. Mesh of Preliminary Model 31

12. Zinc Intensity Mapped onto a SEM Image of CM247LC Bonded at
1214°C for 5 hours. Bondline Indicated by the Yellow Arrow 34

13. Area Scan of Rene 80 Bonded at 1214°C for 3 hours 35

14. The Natural Log of the Weight Percent vs. Distance from the
Bondline Squared for Rene 80 Bonded at 1214°C for 3 hours 38

15. Schematic Showing Locations of ‘Center’ and ‘Edge’ 40

16. Maximum Stress at the Bondface vs. the Number of Nodes in the Model 49

17. a) Meshed Model Used for Simulation of CM247LC and Rene 80 Bonding b) Meshed Model Used for Simulation of APMT Bonding 50

18. a) Normal Stress Distribution and b) von Mises Stress Distribution at the Bondface at 1200°C for CM247LC 52

19. a) Normal Stress Distribution and b) von Mises Stress Distribution at the Bondface at 1200°C for Rene 80 53

20. a) Normal Stress Distribution and b) von Mises Stress Distribution at the Bondface at 1200°C for APMT 54

21. a) Normal Stress Distribution and b) von Mises Stress Distribution at the Interface of APMT and Rene 80 for the Bonding of APMT at 1200°C 55

22. Schematic of Simplified Model Used for Hand Calculations.....57

23. Boundary Conditions for Rene 80 With Simulated Irregular Jig Contact.....60

24. Normal Stress Distribution at the Bondface at 1200°C for Rene 80 With Simulated Irregular Jig Contact 61

25. von Mises Stress Distribution at the Bondface at 1200°C for Rene 80 With Simulated Irregular Jig Contact 61

26. Boundary Conditions for Rene 80 With Simulated Circular Jig Contact.....62

27. Normal Stress Distribution at the Bondface at 1200°C for Rene 80 With Simulated Circular Jig Contact.....62

28. von Mises Stress Distribution at the Bondface at 1200°C for Rene 80 With Simulated Circular Jig Contact.....63

29. Boundary Conditions for Rene 80 With Fully Supported Hemispheres.....63

30. Normal Stress Distribution at the Bondface at 1200°C for Rene 80 With Fully Supported Hemispheres.....64

31. von Mises Stress Distribution at the Bondface at 1200°C for Rene 80 With Fully Supported Hemispheres.....64

32. von Mises Stress Distribution at the Bondface at 1200°C for Plate That is Stiffer Than the Supporting Material 68

LIST OF TABLES

Table Page

1. Composition (wt%) of Superalloys Used in this Study [34, 35] 21

2. Distance from the Bondline to Area Analyzed with Distance Squared Values and Natural Log of Weight Percent for Rene 80 Bonded at 1214°C for 3 hours 38

3. Diffusion Coefficients and R^2 Values for All Collected Samples 39

4. Approximate Mass of Zinc Diffused into Bonded Samples 41

5. Centerline Composition of Each Joint (wt% Zn) 41

6. Coefficients of Thermal Expansion for Parent Materials 47

7. Coefficients of Thermal Expansion for Steel 47

8. Modulus of Elasticity and Poisson's Ratio Used in Finite Element Model [35, 46-50] 48

9. Results From Mesh Refinement 49

10. Minimum and Maximum von Mises Stresses from Finite Element Models 56

11. Minimum and Maximum Normal Stresses from Finite Element Models 56

12. Maximum Normal and von Mises Stresses from Boundary Conditions Modeling 65

13. Bonding Material Yield Strengths [32, 47, 50] 66

ACKNOWLEDGMENTS

I would like to thank my professors at the University of North Dakota for the aid and support in my graduate studies. I would also like to thank my parents and my sister for always being there for me.

ABSTRACT

The diffusion bonding of Kanthal APMT, CM247LC, and Rene 80 was studied. The objective of the first part of this work was to create diffusion bonded test samples of Kanthal APMT, CM247LC, and Rene 80 using a 25μm thick zinc interlayer at varying times and temperatures. Then, using scanning electron microscopy to determine the profile of the zinc diffusing into the parent materials, the diffusion coefficients of the zinc interlayer into the materials were determined for each of the materials at each bonding time and temperature. The next objective was to create a finite element model of the bonding process to determine the stresses present at the bondface at the bonding temperature. A model of the geometry used to create the diffusion specimens was created in ANSYS Workbench 14.0. The stress distributions of the model at the bondface were compared to other research of similar bonding conditions to validate the model.

The diffusion coefficients of the materials found for the APMT and Rene 80 followed the expected trend of decreasing as the bonding time increased. It was also observed that the approximate amount of zinc at the bond region decreased from the center to the edge of the bond supporting the theory of evaporative metal bonding. In addition, the nickel based alloys, CM247LC and Rene 80, had diffusion coefficients that approached theoretical diffusion coefficients of zinc in

pure nickel. The finite element model showed stress distributions that qualitatively agreed with those reported in other studies although there were some discrepancies. However, it was determined that these were a result of the geometry of the jig used to hold the samples in place for bonding.

CHAPTER I

INTRODUCTION

Project Purpose

Fossil fuels continue to be a major source of energy production all over the planet. However, the increased concern over greenhouse gases and other emissions from powerplants has the industry researching cleaner methods of power production. One of these methods is high hydrogen gas turbines combusting gasified coal [1]. The components of these turbines have traditionally been made of nickel or cobalt base alloys and protected with thermal barrier coatings (TBCs). The coatings' purpose is to keep the temperature of the component material down and to help prevent hot corrosion and oxidation of the component materials [2]. By preventing the corrosion of the turbine components, the service life of the turbine increases drastically [3].

In service, failure of the part is generally defined as when the TBC fails and exposes the base material to the corrosive environment inside the turbine. The primary failure mechanism of TBCs is spallation, which is when fragments of the material are ejected from the part due to stress or impact. The spallation life of the TBC varies based on the adhesion level of the TBC to the part to which it is adhered [4]. Greater spallation resistance will lead to a longer life for the part. In addition, because some of the components, such as the turbine blades, are

subjected to continuous stresses at high temperatures, the component materials (parent materials) need to have adequate creep strength to prevent failure of the component [2,3].

Overview of Diffusion Bonding

Diffusion bonding is a process in which materials are joined together through the diffusion of the atoms in the system rather than the melting of the materials to be joined as in fusion welding. Because the materials being bonded in diffusion bonding do not experience bulk melting, the microstructure of the material is largely preserved. This means that materials like nickel superalloys that get a large portion of their high temperature strength from their microstructure can be bonded and potentially retain their creep resistance. Some big advantages of diffusion bonding are the ability to make near net shapes, cause minimal change in material properties, bond together dissimilar materials, and fabricate internal structures [5, 6].

The process of diffusion bonding can be simplified to two stages. First, the two materials must come into intimate contact with each other. The reason that the contact must be extremely close is so that the atoms can diffuse across the joint to form a homogenous bond of the materials. If the materials to be joined are not brought into close enough contact, the material will not be able to diffuse, leaving voids in the bond region and leading to a weak joint [5]. To achieve this intimate contact, the bonding surfaces must be relatively smooth and clean. The parts are first machined to achieve the desired flat surfaces. After being

machined, each of the surfaces must be cleaned to remove contaminants and oxidation, which can form impurities in the joint. One method for cleaning is using an acid bath so as to free the surface of any oxidation or other material imperfections, depending on the reactivity of the material [5]. The pieces to be joined are then placed within a jig and clamped at a high pressure. The clamping pressure not only brings the materials into the desired intimate contact but may also yield some of the microscopic ridges on the interface to form a more intimate bond interface [7]. Figure 1 shows a representative drawing of two materials coming together a) just after the materials are placed together without the clamping force and b) after the clamping force is applied and the materials have yielded at the bondface. It can be seen that the clamping force brings more parent material into contact and reduces the size of the voids at the interface.

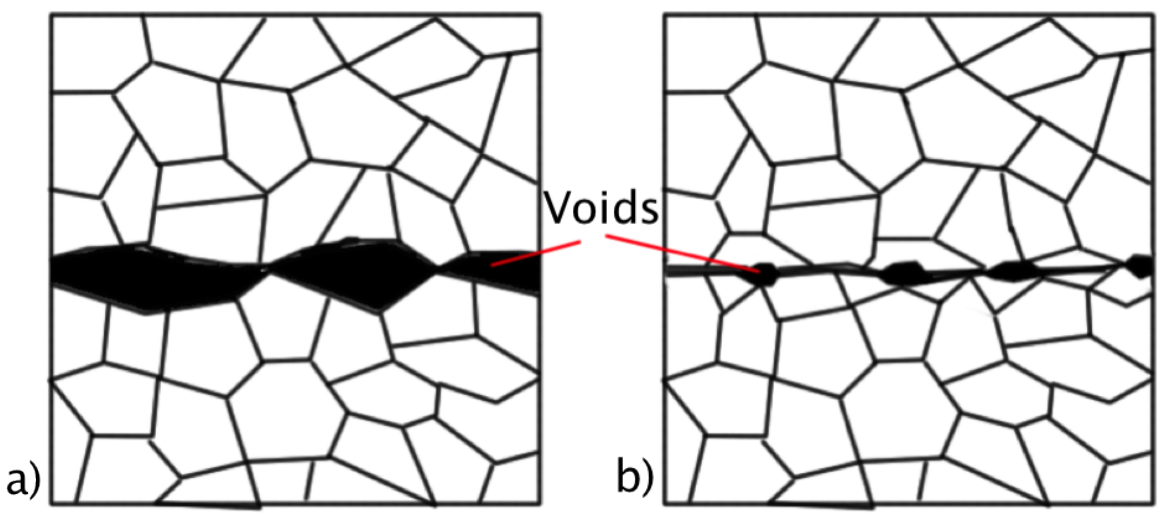

Figure 1. a) Voids Present During Initial Contact Between the Materials b) Voids Present After the Clamping Force is Applied

If an interlayer is used in the bonding process it may also aid in achieving intimate contact. The interlayer material can fill the remaining small irregularities on the bond interface, depending on the clamping force and interlayer properties.

The second and most important stage of the bonding process is the diffusion of the atoms across the boundary between the parent materials typically facilitated by elevated temperature. The pressure applied to achieve better contact of the materials to be joined not only facilitates the interface matching but it also adds to the bond interface stress gradient, which will cause some initial migration of atoms across the interface [8]. To prevent the oxidation of the samples that would otherwise create imperfections in the bond, most materials are bonded under high vacuum or inert environments ranging from hydrogen to nitrogen [7]. To achieve the appropriate environment, the bonding is done in an environment-controlled furnace. The bonding temperature and the time at the bonding temperature vary depending on the materials that are being bonded. Bonding temperatures tend to fall in the range of 50% to 90% of the parent material's melting temperature [9]. The elevated temperature facilitates the bonding because it adds the necessary energy to the system such that the atoms can move relatively freely.

The use of an interlayer not only facilitates the contact between the materials but also is the main mechanism for the diffusion of atoms in the actual bond. The diffusion of the atoms of the interlayer into the parent material acts in a manner similar to a catalyst for the movement and diffusion of the parent material [5]. The atoms of the interlayer diffuse into the parent material creating joining the

parent material to the interlayer. To achieve greater strength of bonding, atoms of the parent material must diffuse across the interface and interdiffuse with the parent material on the other side of the bondline, creating a more homogenous joint [10]. The interlayer atoms then form second phase particles, form solid solutions, or diffuse out of the parent material [11]. When the interlayer diffuses out of the parent material this is referred to as evaporative metal bonding. Figure 2 shows a representation of evaporative metal bonding where the parent material is shown in blue and an exaggerated interlayer is shown in red. The black lines represent the diffusion path of the interlayer where it diffuses into the parent material before diffusing to the edge of the sample and evaporating out of the system. This is beneficial because the interlayer cannot form unwanted second phases [12].

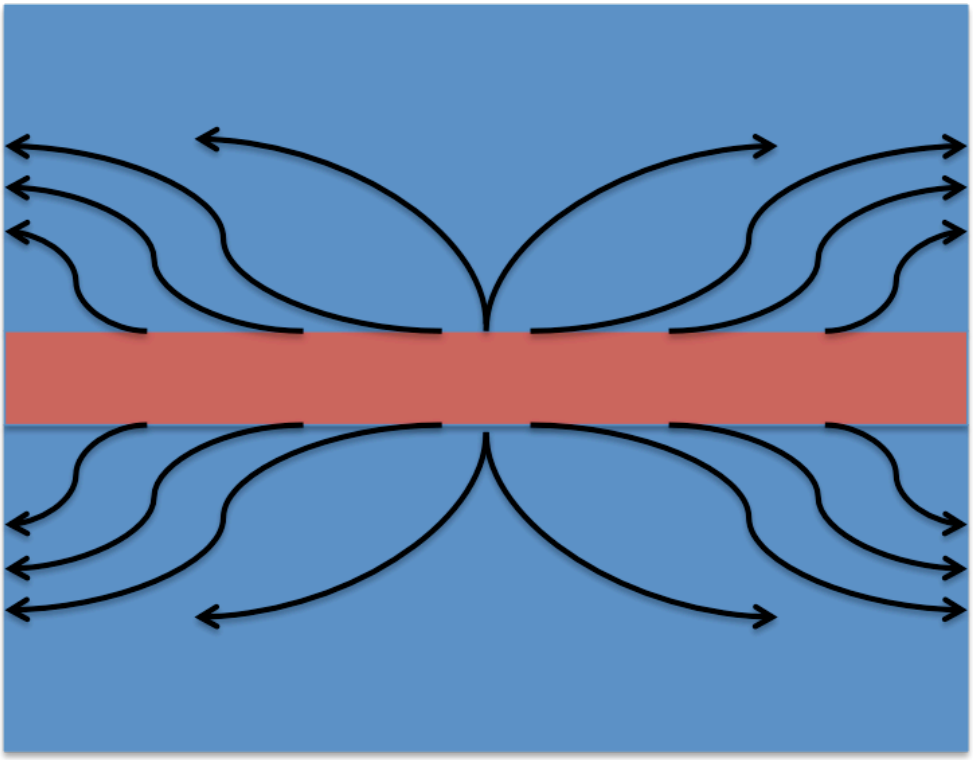

Figure 2. Diagram of Interlayer Movement in Evaporative Metal Bonding

Prior Work

Prior Work Overview

Superalloys are metal alloys that have been specially engineered so as to have superior strength and creep resistance at elevated temperatures. With the introduction of superalloys in the manufacture of turbine components in the 1940s, the life of the turbine discs and other parts increased dramatically [13]. The base element of these alloys can be nickel, iron, or cobalt with alloying elements of chromium, molybdenum, tungsten, and other various metals. As superalloys have a very specific grain structure, joining them with standard fusion welding is quite difficult because the heat involved destroys the microstructure that gives the superalloy its strength at elevated temperatures. By utilizing diffusion bonding, superalloys can be bonded together and still preserve their microstructure and therefore maintain their high temperature strength [14]. With the increased use of superalloys in industry, research into the diffusion bonding of them is becoming more prominent.

A great deal of research is being done into the different parameters involved with the diffusion bonding of different materials, from the bonding temperature to the time at the bonding temperature to the pressure at the joint interface. The temperature and the bonding time are highly dependent on the materials being bonded [7,10]. Bonding temperatures for diffusion bonding can be as low as 400°C [10] and can be over 1300°C depending on the materials being joined [7]. Similarly, joining times can vary from a few minutes to hundreds

of hours [7]. The bonding time and temperature are important variables in the diffusion process; if the temperature is too low there will not be enough energy in the system for the atoms to move across the bondline. As the temperature increases, the isothermal solidification rate decreases which decreases the time required to create a uniform bond. Likewise, if the bonding time is too short, isothermal solidification can not be completed and the joint can be brittle and weak [15]. If the time is too long and the diffusivity of the bonding materials is significantly different, it is possible for the material with the higher diffusivity to diffuse into the other material faster causing Kirkendall voids to form [7,15]. For these reasons, each combination of metals to be bonded must be studied to determine ideal process conditions. Numerous studies have been done on the effects of different bonding parameters on the bonding of superalloys. These studies tend to focus on the pressure at the bondline and its effect on the quality of the bond as well as the effect of the temperature cycle used to make the bond on the strength of the alloys. The effects of bonding pressure and the effect of the bonding process on the material are the most studied because they are the most universal across the different materials being used [15-22].

Bonding Pressure

The pressure at the bond interface can have a great effect on the diffusion of the materials across the bond interface. The pressure used for the bonding can yield the bondface, which creates better contact between the two parts. The more intimate the contact between the parts, the easier it is for atoms of the

materials to diffuse across the joint. However, the optimal surface finish for bonding is not necessarily perfectly smooth. Leaving some surface roughness allows for yielding of the materials at the bond interface [7]. The yielding creates distortion energy at the bonding region; this additional energy lowers the activation energy of diffusion and creates some heat which means that less energy has to be added to the system for bonding to occur [15]. Studies show that the increase of pressure at the bonding interface decreases the voids present at the bond and increases the strength of the bond. However, the increase of bond quality as the pressure increases does have its limit. Depending on the materials being bonded, the strength of the bond will reach a limit at which the strength no longer increases with the increase of bonding pressure [14-17].

Saha and Kahn studied the effect of changing the pressure on the bondface during the bonding of nickel superalloy Inconel MA 758 to itself. They found that increasing the pressure decreased the width of the joint. Through microhardness tests, it was determined that the joint region formed with this alloy and interlayer combination is weaker than the parent material so the strongest joint will be that with the smallest bonding zone. Once the bonding pressure got above 2 MPa, the width of the joint no longer decreased [14].

In the study by Hong Li and Zhuo-Xin Li the strength of diffusion bonded of steel panels was measured. The specimens were varied with reference to the amount of plastic deformation that the materials underwent at bonding. The plastic deformation here is measured by the reduction percent of the original thickness of the specimens. In this study the increasing of the plastic deformation

is comparable to the increasing of pressure at bonding that was applied in other studies because to achieve a greater amount of plastic deformation (percent reduction) a greater force must be applied. The sample materials in this study the maximum stress in joint needed to exceed the yield strength of the material so the stress at the bondface exceeded 210 MPa. It can be seen in Figure 3 that with the increase in reduction percent of the sample that the strength of the bond increases until a maximum after which the strength of the bond no longer increases [15].

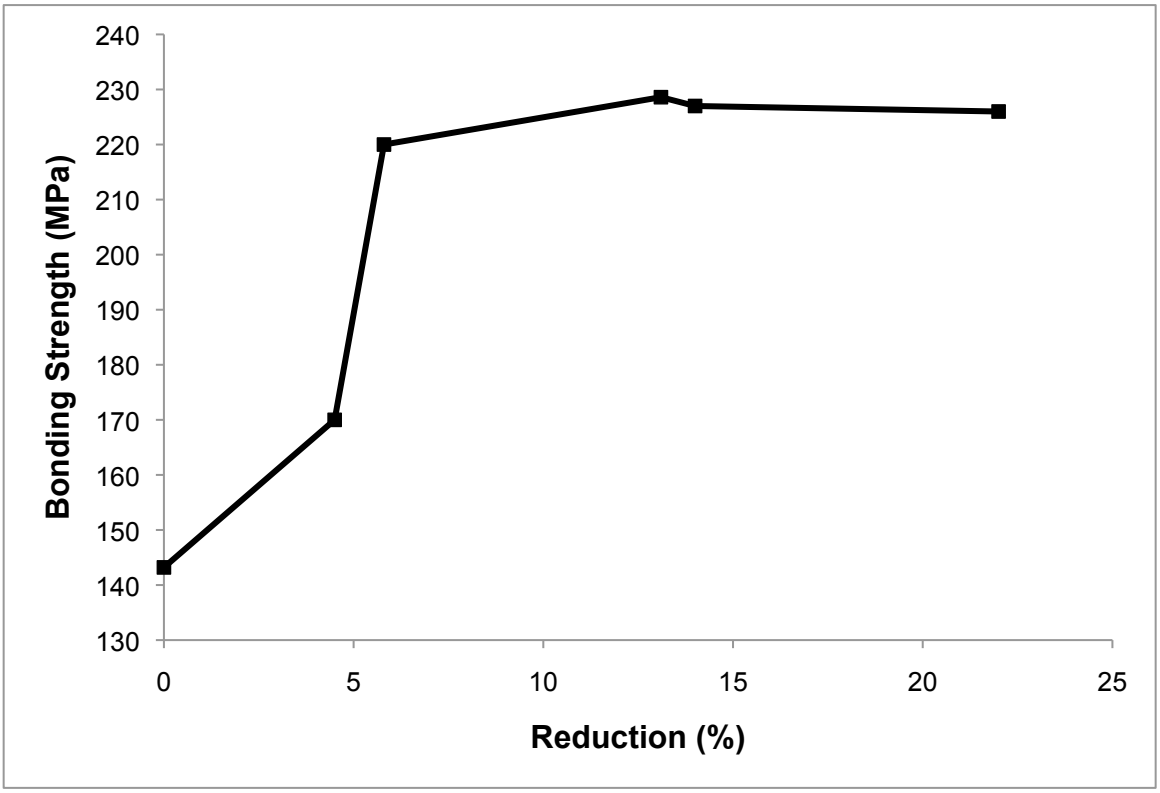

Figure 3. The Effect of Reduction Percent on Bonding Strength [15]

Other researchers also performed studies that measured the bonding pressure by relating the bonding pressure to the deformation of the original

materials [16, 17]. In each of these studies, the strength of the bond increased as the bonding pressure increased up to a maximum. However, the pressure at the bondface for the optimal strength varies depending on the materials being bonded. The pressure can be larger than the yield strength of the material and permanently deform the material [15] or be as low as 15% of the yield strength and cause no permanent deformation [17]. Even though the materials being bonded, the bonding times, bonding temperatures, and bonding pressures varied the same conclusions were made: 1) the quality and strength of the bond increased with increasing bonding pressure and 2) after a certain point increasing the bonding pressure no longer increases the strength of the joint [14-17, 23]. While the maximum strength of the joints remained relatively constant at its highest point over each of the studies, Zhang and Chandel noted that at elevated pressures and higher temperatures a microstructure was observed at the bond interface that may degrade the bond strength. However, a joint strength of 95% of the parent material strength at room temperature was still observed with the noted microstructure [17].

Another advantage to the increase in bonding pressure is the effect it has on the impurities of the bond itself. Other researchers looked at the change in the quality of the bondline as the pressure was varied. One such study found that with the increase of the pressure of the bonding the amount of defects in the joint was reduced. One explanation of this is that compounds that have a low melting temperature are being squeezed out of the bond taking unwanted oxides with them [14]. The increased pressure may also decrease voids in the joint. The

voids shrink for various reasons at the increased pressure. Increasing the pressure at the bondface causes more local yielding. Bondface yielding brings the surfaces closer together by reducing the surface roughness through yielding the peaks of the roughness [7]. The pressure can also plastically deform the interlayer, pushing it into the surface scratches, which adds to the area of atoms that can diffuse because they cannot diffuse across empty space. The yielding not only brings the faces into closer proximity to each other but also creates distortion energy that makes it easier for diffusion to occur [15].

Bonding Temperature

An area of large concern with diffusion bonding is the effect on the parent material caused by the heating cycle used in the diffusion bonding process. Nickel-based superalloys get their desirable properties not only from their combination of elements but also from the microstructures of the compounds present in the alloy. The microstructures are largely determined by the way that the superalloy is solidified as well as any heat treatments applied to it after the initial casting [24]. By heating the part up to the point where atoms of the interlayer and bonding materials can diffuse, the atoms in the microstructure can diffuse to form secondary phases with the interlayer material or desired second phases can precipitate out of the material [18]. The microstructure created by the diffusion bonding process at and around the bondline can be quite different than that of the original unbonded material. As shown in Figure 4 [19], the bond interface may have a higher hardness than the surrounding material. It can also

be seen that heat-treating the part after the bonding is completed has been shown to create a uniform hardness across the bond in some materials [19,20].

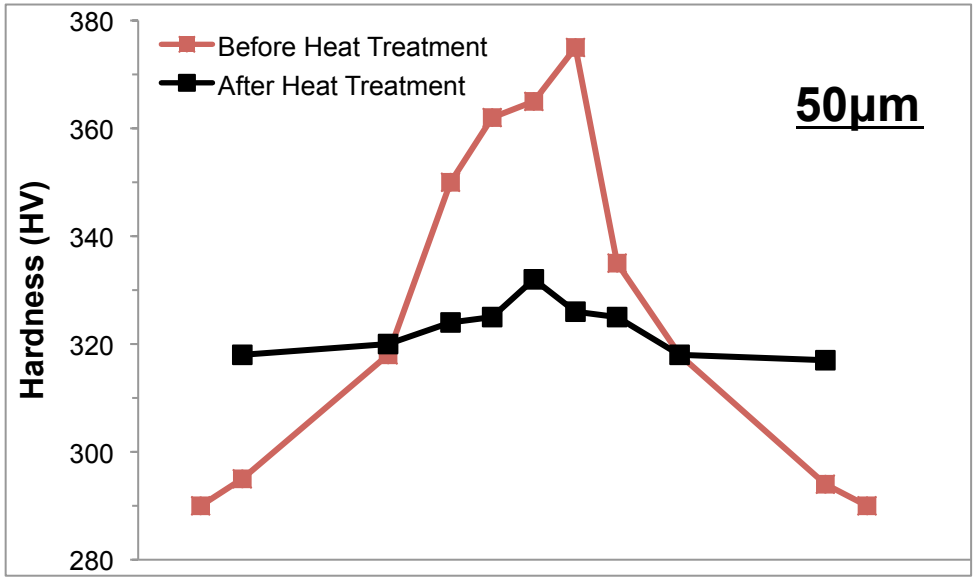

Figure 4. Hardness Distribution in a Diffusion Joint Before and After Heat Treatment Across the Bondline [18]

Studies on the heat treatment of specific superalloys have been conducted after diffusion bonding and on the as-cast material. These studies show that for the superalloys Rene 80 and CM247LC, performing a post-process heat treatment can increase the strength of the material or, in the case of diffusion bonded parts, return their strength to that of the pre-bonded alloy [20-22]. Depending on the interlayer used, the structure of the bond region varies. A study was done on the post bonding heat treatment of Rene 80 joined using a nickel-based interlayer. The specimens were bonded under vaccum at 1100°C for 60 minutes. After bonding, the specimens were cooled to room temperature then a post-bonding heat treatment of 2 hours at 1206°C was performed. As shown in Figure 5a, it can be seen that for the given bonding conditions and

materials, the interlayer formed undesirable intermetallic compounds at the bondline causing the grain structure to be discontinuous. However, in Figure 5b it can be seen that after a heat treatment the grain structure reforms and the intermetallics have been removed. Strength testing was also done on the bonded specimen after the material had passed through the heat treatment and it regained its strength to over 90% of the base metal at room temperature [20].

a)

b)

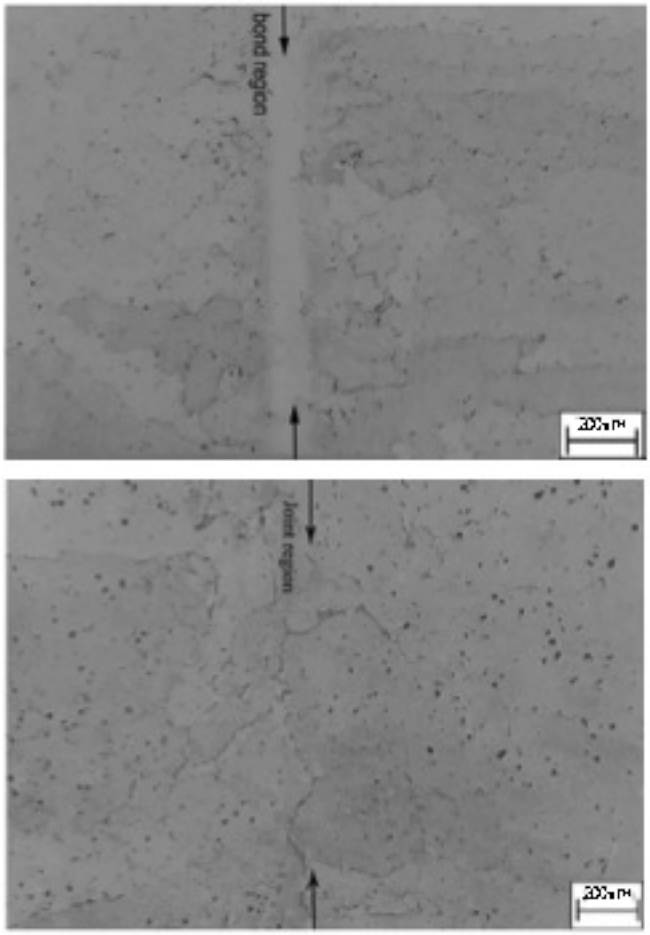

Figure 5. Microstructure of Rene 80 a) As Bonded b) After Post Bonding Heat Treatment. [20]

Finite Element Modeling

With the rise in the use of diffusion bonded parts, more research is being done on the finite element modeling of the diffusion bonding process and

diffusion-bonded joints with the goal of creating stronger joints and more complex geometries of diffusion-bonded parts. Much of the finite element models use data gathered from the bonding materials and interlayers to model the diffusion of the atoms and their formation of secondary phases [25, 26]. This type of modeling is beyond the scope of the current research project. The model to be made in this project will focus on the stresses at the bond interface during the bonding process.

One major issue with modeling diffusion bonding comes from the thermal expansion of the parent materials being bonded. As it is possible to bond two different materials together with diffusion bonding, the difference in material properties must be carefully noted. The materials being bonded may not have thermal expansion coefficients that are even relatively close to each other. Additional stresses can arise from the differences in thermal expansion of components and must be included in the design of the final part [27]. These stresses arise from the materials expanding during heating, then bonding at the elevated temperature and contracting during cooling to ambient temperature. The bond is created at a point in which the materials have expanded; if they have expanded unevenly due to different coefficients of thermal expansion, when the materials cool residual stresses will arise from the uneven shrinkage across the newly bonded part [23, 28-30]. In some cases, the stresses are large enough that the parent material can fracture due to the residual stresses. For these cases researchers have found that sandwiching additional layers between the materials to be bonded can aid in reducing the stress. By using materials of different

thermal expansions and elastic moduli, it is possible to reduce the residual stresses so as to prevent the failure of the parent materials [30, 31].

Whether or not the materials have the same thermal expansions, there are likely to be residual stresses at the bond interface. This stems from the fact that the solidification of the entire joint does not happen at once but may occur while the part is still heating or is cooling and will therefore be expanding or contracting. These residual stresses must also be accounted for in the model [23, 32]. Figures 6 a&b [32] show the residual axial stresses formed from the bonding of Al_2O_3–TiC to itself using W18Cr4V as a sandwich layer. The model is a 2-D axisymmetric thermal model of the bonding specimen. The 2-D section used to create the model is shown in gray in the 3-D sketch of the bonding setup in Figure 6a. The model was constrained such that the all the nodes on the left of the model were constrained in the radial direction and all of the nodes in the bottom were constrained in the axial direction. An external uniform pressure was applied to the top edge and an initial temperature of the model was applied then the model was cooled to ambient temperature. In Figure 6b, from the figure it can be observed that the stress is uniform across the bond out to near the edge of the bond where increases to the maximum before the decreasing to a minimum at the edge of the sample [32]. However it can also be seen that the stress distribution in the model is not the same in the top layer of Al_2O_3-TiC as in the bottom. This is probably due to the constraints used in the model. This model shows the residual stresses after the bonded specimen returned back to ambient temperature. The residual stress in the model is an artifact of the high pressure

and plastic deformation of the material near the interface of the materials. Where a larger compressive load leads to larger compressive plastic deformation, which will then lead to a larger tensile residual stress.

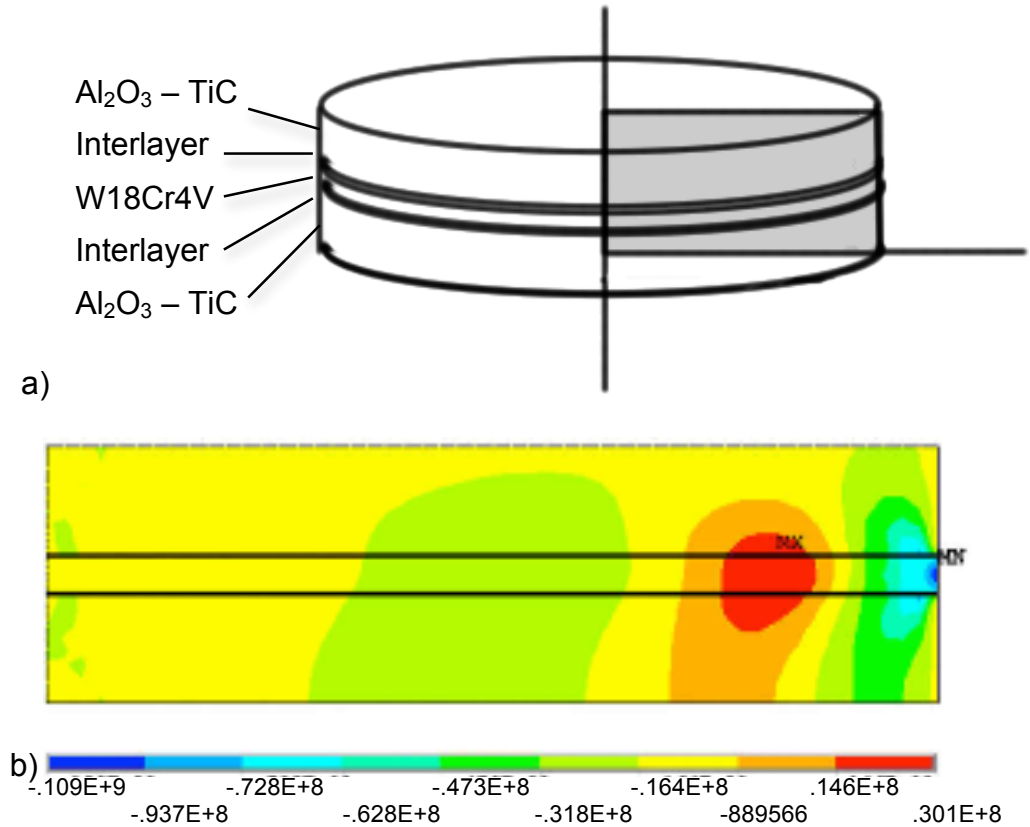

Figure 6. a) Diagram of Diffusion Bonded Joint b) Distribution of Residual Axial Stresses (in Pa) [32]

For the cases were the materials being bonded have different material properties, the combination of materials being bonded does not have an affect on the appearance of the stress distribution profile. Each study showed that for samples of different material properties, the stress at the bondface is relatively constant from the center of the bond before increasing just ahead of the outer edge of the sample then reducing to a minimum at the edge of the bond [23, 28-

30, 33]. The shape of the bondline stress profile is consistent across material systems, but the magnitude of the stress varies depending on the materials used.

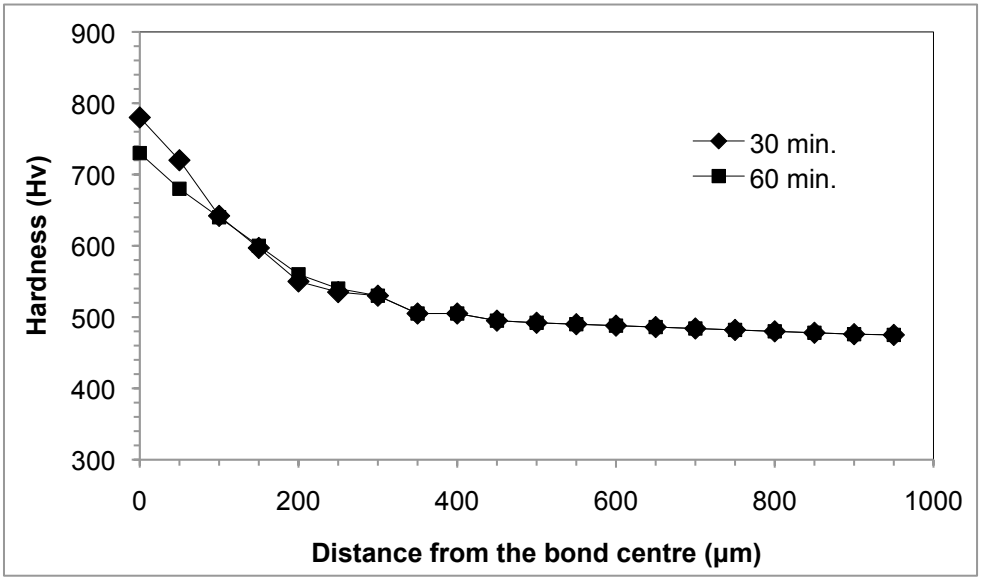

Figure 7. Hardness of Rene 80 Versus Distance from Center of the Bond [20]

The stress profile of joints made between like materials is different from that of joints made between different materials. As can be seen in Figure 7 [20] the hardness at the center of the bond is the greatest and decreases further from the center. One explanation for this is that the hardness at the center of the bond can be related to greater yield strength and the greater yield strength attributed to smaller grain size from the reverse Hall-Petch relation. The smaller grain size can be credited to greater pressure during solidification of the bond [33]. Therefore in a bond of like metals it is plausible that the pressure at the center of the specimen during bonding will be the greatest and the pressure will be decreasing to the minimum at the edge of the sample, although it remains constant across majority of the bond. Another explanation for the increased

hardness at the center of the bond is materials from the interlayer forming additional phases [20].

The residual stress at the bondface is beneficial to modeling of the diffusion-bonded part. Knowing that the general distribution of the residual stress on the diffusion bonded face is consistent across many different bonding conditions allows for the verification of the finite element model [32]. If the generated finite element model has a stress distribution similar to that of the previous research it can be assumed that the model is an accurate representation of the bonding process.

Current Work

Through a grant from the Department Of Energy (DOE) the Mechanical Engineering Department at the University of North Dakota, in conjunction with the University of North Dakota Energy & Environmental Research Center (EERC), studied the diffusion bonding of Kanthal APMT, CM247LC, and Rene 80 with the goal of designing turbine engine components with better mechanical properties than those currently being produced. The objective of the first part of this work is to create diffusion bonded joints of Kanthal APMT, CM247LC, and Rene 80 using zinc as the interlayer for the bonds then use scanning electron microscopy to determine the diffusion coefficients for the materials. The other objective is to build a finite element model of the samples during the bonding process with the intent of the model being used to help design a fixture to bond Kanthal APMT to CM247LC or Rene 80 with complex geometries. The coefficients of thermal

expansion of the materials for use in the finite element model will be determined using a thermal mechanical analyzer (TMA). The method for the creation of diffusion-bonded specimens and results of the diffusion of the interlayer as well as the creation and verification of a finite element model of the bonding process will be discussed in subsequent chapters of this thesis.

CHAPTER II

METHODS

Overview

The superalloys CM247LC, Rene 80 and APMT were each to be bonded to themselves using zinc foil as the interlayer. The time at the bonding temperature as well as the bonding temperature were to be varied. The diffusion distance of the zinc was then to be measured so as to determine the diffusion coefficients of the zinc in the superalloys. Next, a finite element model of the bonding of the samples was to be constructed. The material properties at high temperatures were to be measured to serve as the material constants put into the computer model. With the diffusion coefficients of the materials and an accurate finite element model of the bonding stresses and it should be possible to design a fixture for the bonding of more complex turbine components that have a core of high creep strength CM247LC or Rene 80 coated with spallation- and oxidation-resistant APMT.

Material Selection

Bonding Alloys

The materials that were used for bonding in this research were Kanthal APMT, CM247LC, and Rene 80. The composition of the bonding materials is shown in Table 1.

Table 1. Composition (wt%) of Superalloys Used in this Study [34, 35].

	Cr	C	Mo	W	Ti	Co	Al	B	Zr	Hf	Mn	Si	Ta	Fe	Ni
APMT	23.5	0.08	3	-	-	-	5	-	-	-	0.4	0.7	-	Bal	-
CM247LC	8	0.07	0.5	10	0.7	9	5.6	0.015	0.01	1.4	-	-	3.2	-	Bal
Rene 80	14	0.16	4	4	5	9.5	3	0.015	0.03	-	-	-	-	-	Bal

These materials were selected because of their use in previous related research and their current use in high temperature environments [36]. Previous research conducted by John Hurley has found that the superalloys CM247LC and Rene 80 have superior strength at high temperatures to Kanthal APMT. It was also discovered that Kanthal APMT had a TBC spallation life three times that of CM247LC and Rene 80 and is much more oxidation-resistant, as well [12]. Increasing the spallation life and oxidation resistance of turbine components increases the time it to failure of the components, which increases the turbine maintenance intervals [37-39].

Previously, samples of CM247LC were diffusion bonded to Kanthal APMT. It was observed that the materials formed a uniform bond and, when creep tested, all of the specimens failed within the Kanthal APMT region away from the bondline [12]. The creation of turbine components with spallation- and oxidation-resistant Kanthal APMT bonded over a core of CM247LC or Rene 80, which have better creep strength, has the potential to produce turbine components that have vastly longer lives than those of parts made with just one alloy.

Interlayer

The interlayer used for the bonding of all of the materials was a commercially pure thin zinc foil. Zinc was selected as the interlayer for multiple reasons. First, zinc has a relatively low melting temperature compared to the alloys to be bonded. A molten interlayer is not necessary for bonding. However, a molten interlayer will aid in filling any remaining voids at the bond interface [9]. The low melting temperature of zinc makes the diffusion of the zinc energetically favorable; this is because the liquid zinc has a lower activation energy than solid zinc and so can diffuse through the parent materials easier. Second, zinc has a high vapor pressure; this is favorable because once the zinc diffuses through the joint and to the edge of the material it will evaporate off of the surface and thus not form second phases in the parent materials. Zinc was also used in the previous study when CM247LC and Kanthal APMT were bonded and a good joint was created [12,36].

Other Metals

For the actual bonding process, the samples were placed in a jig as shown in Figures 8a&b. The fixture, as well as the bolt that hold the sample in place, were machined from commercially pure molybdenum and the articulating hemispheres were made of AISI E 52100 high carbon steel. The molybdenum was chosen because the bonding materials have a greater coefficient of thermal expansion meaning the materials to be joined will create greater pressure at the joint following thermal expansion, which should create better contact between the

two pieces leading to a better bond. Molybdenum was also because it has good high temperature strength. The threads used on the jig and the bolts were Acme 1/2”-10 threads. These threads were chosen so that the bolts are able to withstand higher loads without failure. Trapezoidal threads are typically used in applications where large loads are present. They are able to sustain greater loads because the base of the tooth is wider than triangular threads and therefore can withstand greater loads [40].

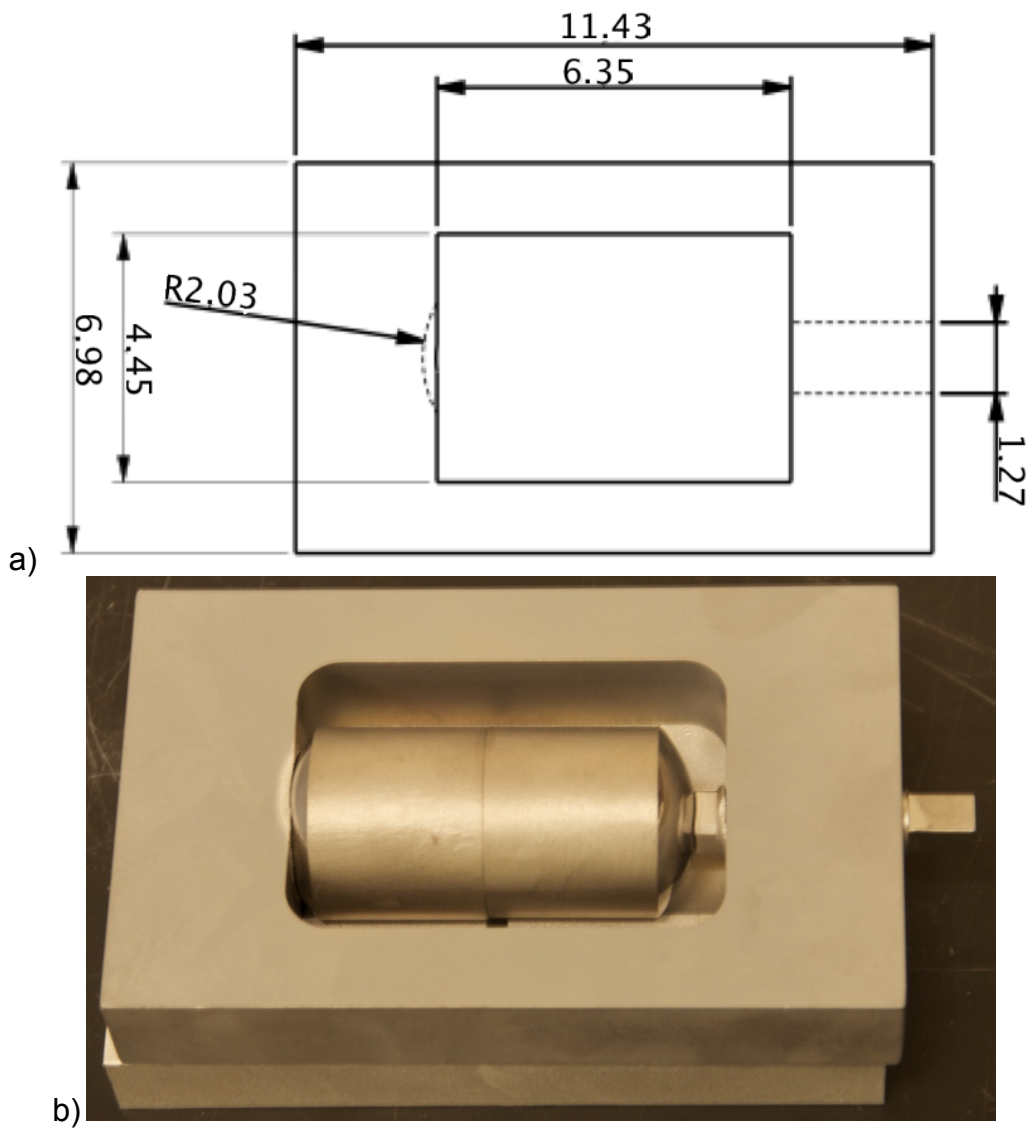

Figure 8. a) Bonding Jig Fixture Geometry (units in cm)
b) Assembled Bonding Fixture

The end of the bolt is concave such that it mates well with the steel hemisphere. The high carbon steel was chosen because it is strong, inexpensive, and commercially available in spheres. By getting the steel in larger spheres, six hemispheres with a high quality surface finish can be obtained per sphere. The hemispheres insure that the pressure applied from the fixture is applied perpendicular to the bond interface allowing for intimate contact between the parts, which should create a better bond.

To prevent any residual stresses in the fixture from the machining process, the fixture was made utilizing electrical discharge machining. The samples to be bonded were electrical discharge machined to 2.54 cm long from the 30.48 cm long, 2.79 cm diameter bars received for the CM247LC and Rene 80. For the APMT, 3 mm thick 2.79 cm diameter discs were produced from the 3mm thick received APMT plate. The interlayer used was commercially pure zinc foil 25 microns thick from ESPI Metals of 1050 Benson Way Ashland, Oregon 97520.

Creation of Diffusion Bonded Samples

After sample parts were machined to size, the bond faces were ground with 180 grit silicon carbide paper achieving a surface roughness of approximately Ra=0.8 micron [41] on a MetPrep 3 PH3 sample polishing machine to insure flat bonding surfaces. Next, each of the samples as well as the fixture, bolts, and hemispheres were sandblasted with silica sand to remove any surface oxidation that may have accumulated and may cause impurities in the

bond. The samples were then ground again on the bonding face with 220 grit silicon carbide paper on the sample polishing machine. Everything was then subsequently cleaned for 1 hour submerged in acetone in a Branson 5510 ultrasonic cleaner. After the ultrasonic cleaning, each piece was taken out of the acetone, cleaned again with isopropyl alcohol, and assembled in the fixture as shown previously in Figure 8b. In the case of the APMT samples, Rene 80 was used as plugs to hold the APMT samples in place. Each sample to be bonded is placed in the fixture and secured in place by the threaded bolt and a torque of 2.26 Newton*meters was applied to the bolt.

Once assembled, the excess zinc foil was trimmed from around the bond interface, the entire fixture was again cleaned with isopropyl alcohol and the entire fixture was placed into an Orton tube furnace that allows for the temperature and atmosphere to be controlled. Once the samples were in the furnace, it was sealed and evacuated to $6x10^{-4}$ mbar with a BMH 70 Dry vacuum pump. The chamber was then flooded back to 0 kPa gage pressure with commercially pure argon that was additionally filtered by a Trigon Technologies Hydrocarbon Trap, a Trigon Technologies Big Oxygen Trap, a Flow Glass Moisture Trap, and a Trigon Technologies Indicating Oxygen Trap, to further remove any impurities that may be present in the gas and could possibly react with the bonding materials forming unwanted phases in the bond. The oven was then heated at a rate of 450°C/hr to 700°C and held for 30 minutes, during which the pressure in the oven increased to 100 kPa due to the thermal expansion of the argon in the furnace. This step was implemented with the idea that the

temperature would allow the zinc to melt while under additional pressure so the zinc would not be able to evaporate. The oven was then evacuated and the temperature was raised at a rate of 250°C/hr to the bonding temperature at which it was held for the scheduled time period. The samples were then allowed to cool in the evacuated oven.

After bonding each of the created diffusion samples was sectioned using a Buhler slow speed diamond abrasive saw and subsequently mounted using Buehler EpoxiCure two-part epoxy. The mounted samples were ground to 000 honing paper and then polished to 0.05 micron diamond grit. The polished samples were then analyzed using a Hitachi S-3400N scanning electron microscope (SEM) and energy dispersive spectroscopy (EDS). The samples were then analyzed with area scans to determine the weight percent of areas on the samples. Data was taken at the end of the bond and the center of the bond for each sample. This data was then compiled and used to determine the diffusion coefficient for each of the materials at the tested temperatures and times.

Finite Element Modeling

The other major portion of this research was to make an accurate finite element model of the bonding of the test specimens. In this study an accurate model is defined as one in which the model accurately simulates the stresses at the bonding interface at the bonding temperature. Stress distributions will be determined to be acceptable based on their agreement with stress distributions

reported in other studies. The creation of an accurate model of the test specimens will assist in the creation of a model to simulate the creation of diffusion bonded turbine blades and other turbine components with complex geometries where the core of the part will be made of high creep strength CM247LC or Rene 80 and will have a plating of spallation- and oxidation-resistant APMT diffusion bonded over the whole core. Ultimately the model with the complex geometries will assist in the design of a jig for the bonding of these complex geometries. The stress distribution of a good quality bond will be used as the baseline for what the stress distribution should look like for the design of the new bonding jig.

To create an accurate model of the bonding, the material properties need to be known. The coefficient of thermal expansion was determined to be the most important material property for this finite element model because the pressure at the bondline during bonding is a direct result of the thermal expansion. The coefficients of thermal expansion of each of the materials used were determined experimentally using a Shimadzu TMA 60 thermal mechanical analyzer. To determine the coefficient of thermal expansion, each sample was subjected to a heating cycle where it was heated in 100°C increments in an inert argon gas environment and held at each temperature for fifteen minutes. Every material was tested 4 times and the coefficient of thermal expansion for each temperature interval was averaged across the fifteen-minute time interval and each of the 4 test specimens. The material data was then inputed into the finite element model.

Another parameter that was needed for the model was the preload on the sample. The preload applied to the test specimen was used primarily to hold the bonding samples in place. Pressure sensitive indicating film was used to determine an initial load at the bondface and found a maximum initial pressure of 2.4 MPa. This pressure was determined through the use of Fuji Prescale pressure film made by Sensor Products Inc of 300 Madison Avenue Madison, NJ 07940. Figure 9 shows the pressure film used. The pressure film changes color once a minimum pressure is applied and the color gets darker the more pressure is applied. The film shown in Figure 8 has a range of 0.5 MPa to 2.4 MPa. When the sample was tested using the pressure film that indicates from

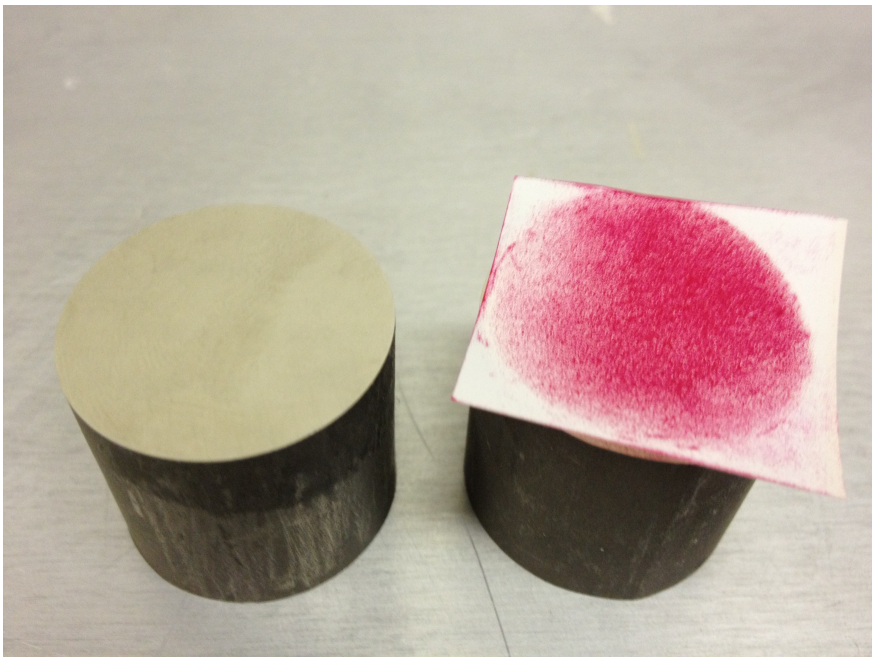

Figure 9. Pressure Film

2.4 MPa to 9.6 MPa the color change in the film was undeterminable so the pressure at the bondface from preload was determined to be an average of 2.4

MPa. It can also be seen in Figure 8 that the stress is not completely uniform but has an area of lower pressure near one side of the specimen. The pressure in this low pressure region was determined to be approximately 1 MPa using the color correction chart for the pressure film. The use of the pressure film not only yielded the preload pressure at the bondface but also confirmed that the grinding schedule produced uniform contact between the samples.

A 3-D solid model was constructed using ANSYS Workbench 14.0. The model was constructed using the “ideal” geometry of each of the parts. The models of the two different test geometries can be seen in Figure 10a&b. Figure 10a shows the setup for the CM247LC and the Rene 80 bonding while Figure 10b is the setup for the APMT. These models have to be different because the APMT received was a plate and slugs of Rene 80 were used to hold the APMT specimens in place. This allowed the same molybdenum jig to be used for all samples.

The model was constrained such that one node on 3 faces of the jig are constrained in one dimension and the hemispheres and test samples were constrained such that the nodes were bonded, behaved asymmetrically and were formulated using Augmented Lagrange, which is a contact formulation that expresses the force between the contact surfaces using both the contact pressure and the normal stiffness of the bodies. The model was constructed to apply thermal loading, at intervals of 100°C, and to show the stresses on the bonding face. Preliminary analysis with representative material property values used for the materials was performed. The setup was meshed with hexahedral

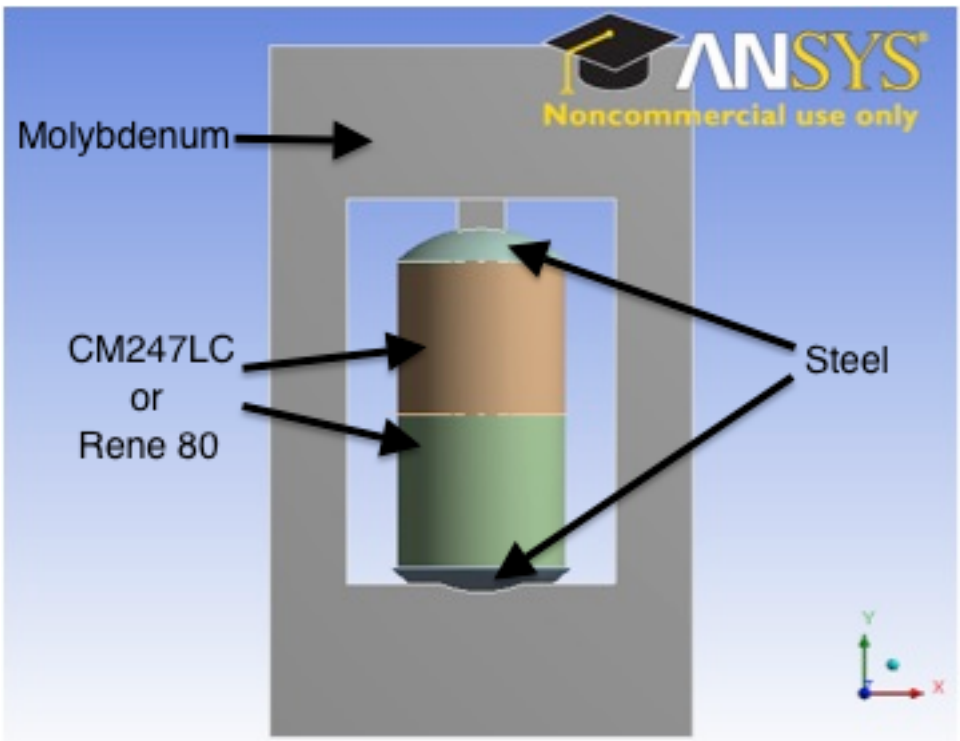

a)

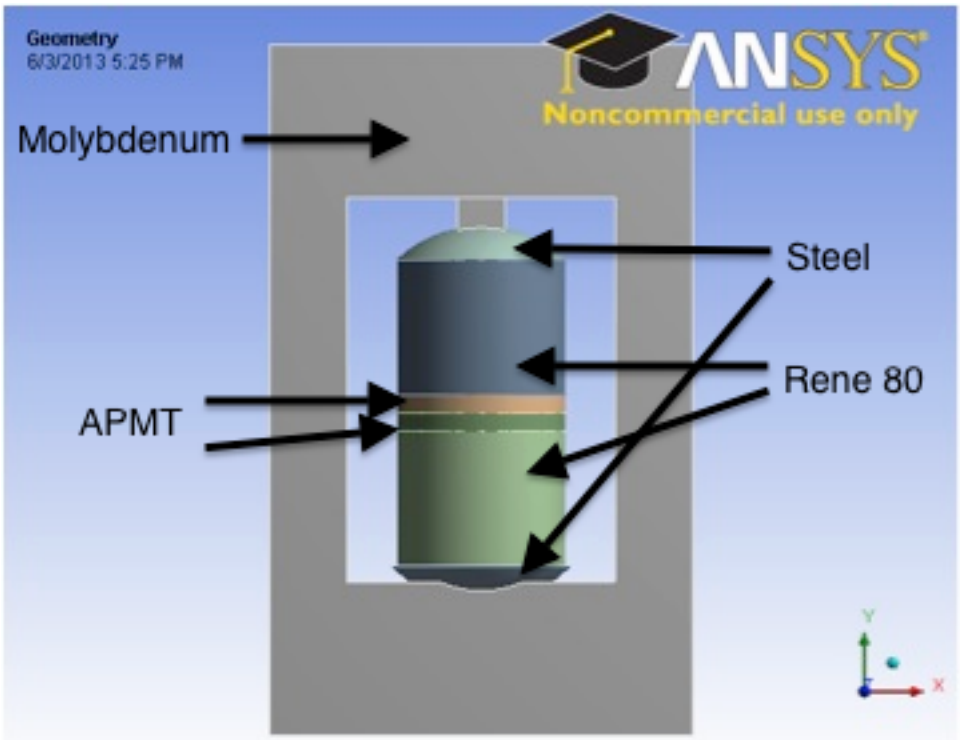

b)

Figure 10. a) Model Used for Simulation of CM247LC and Rene 80 Bonding
b) Model Used for Simulation of APMT Bonding

shaped elements using the fine mesh with a relevance of +80. The mesh size and the relevance both decrease the program-controlled size of the elements in the mesh the relevance. The increased relevance decreases the size of the mesh where a relevance of +100 creates the finest mesh and a relevance of -100 produces the coarsest mesh. The mesh created with these settings for the preliminary model can be seen in Figure 11.

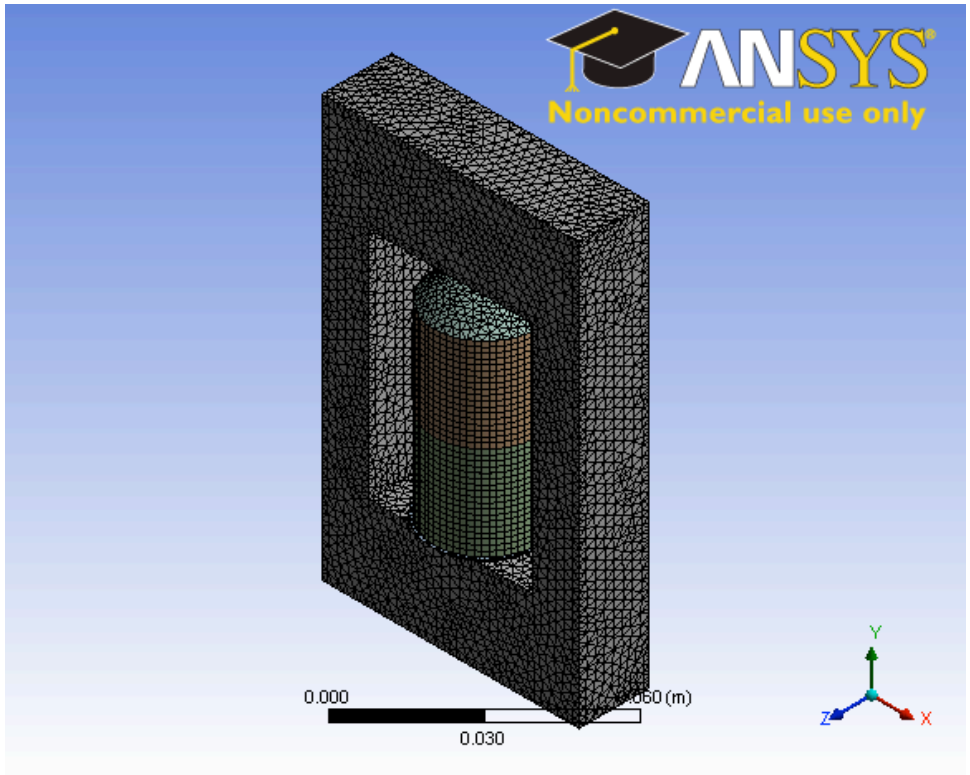

Figure 11 Mesh of Preliminary Model

This preliminary analysis showed that the assumption that the nodes are bonded is valid as the stress distributions for the model visually match the stress distributions of those reported in previous studies [20, 32]. The model was also tested with and without the 2.4 MPa preload on the sample. The high temperature stresses between the model with the preload and with out the

preload varied by less than 0.75%. As a result, the preload was left out of the final model. The assumption of leaving the preload out of the model and using bonded interfaces between the parts will be beneficial to the more complex model as it will make the model simpler and save on computing time. A mesh refinement study was then performed on the model to determine the final mesh size.

CHAPTER III

DATA AND ANALYSIS

Diffusion Data

Diffusion samples were made for time periods of 1, 3, 5, 10, and 20 hours at 1214°C, for 3 and 20 hours at 1155°C, and for 30 minutes at 700°C. Samples were originally also planned for times of 1, 5, 10, and 20 hours for 1155°C as well as for 1, 3, 5, 10, and 20 hours at 1100°C; however, the samples that were created at 1155°C and held for 20 hours did not create a bond. As a bond could not be created for the longest planned bonding time at 1155°C, it was concluded that bonds would not be achieved for shorter periods at the bonding temperature. To save material for future study, these planned samples were not created. It should also be noted that none of the materials bonding experienced any measurable permanent plastic deformation at any temperature and that the APMT samples bonded to the Rene 80 that was used to hold the APMT in place for all cases.

Each of the diffusion-bonded test samples was analyzed with a Hitachi S-3400N scanning electron microscope and the material compositions were determined using energy dispersive spectroscopy. Initially, element mapping was performed on the samples with the zinc being mapped onto the SEM image of the bondline as can be seen in Figure 12. From this preliminary analysis it can be

seen that the diffusion of the zinc through the CM247LC, as well as the Rene 80, and APMT, appears to be bulk diffusion where the zinc diffuses through the whole of the material rather than grain boundary diffusion where the zinc would have diffused primarily along the grains of the material. This is an important observation as the type of diffusion, grain boundary or bulk, defines the equations to be used to determine the diffusion coefficient.

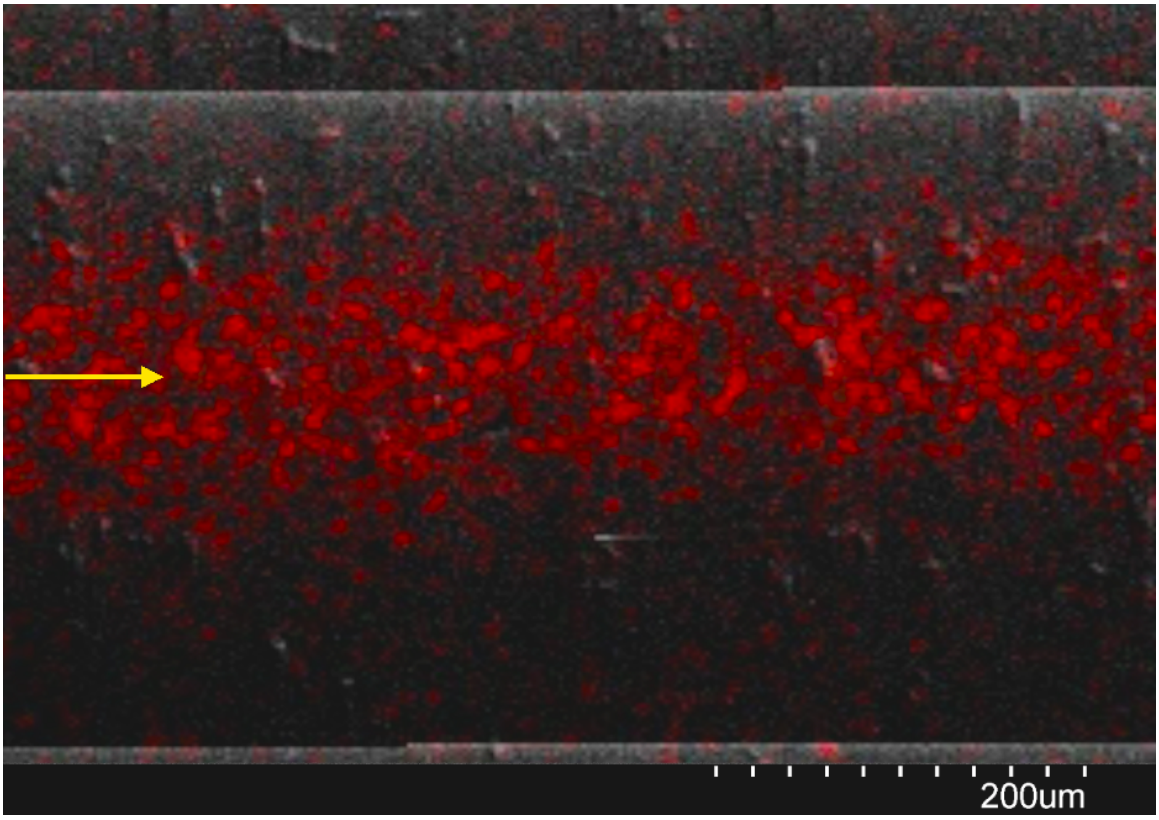

Figure 12. Zinc Intensity Mapped onto a SEM Image of CM247LC Bonded at 1214°C for 5 hours. Bondline Indicated by the Yellow Arrow.

As it appears that the zinc was diffusing through the parent materials via bulk diffusion, the diffusion coefficients of the materials can be determined by knowing the concentration of the zinc as a function of the distance from the

bondline. Area scans to determine weight percent of zinc were performed on each sample. The data was taken by having the EDS measure the weight percent of each of the elements present in the parent material as well as the zinc that is diffusing into the parent material from the interlayer within a specified area. The measurements were taken by specifying equal sized areas side-by-side for the EDS to measure starting at the bondline between the two parent materials and moving farther into the parent material away from the bondline until the level of zinc was less than 0.5% for a minimum of 2 consecutive scans. Each sample was measured at the center of the bondline and at the edge of the bondline (Specimen edge). For the data from the samples that did not bond at all (those that were in the furnace at a bonding temperature of 1155°C or 700°C) area scans were performed at the edge and center of the sample. An example of a SEM image with areas where the EDS measurements were taken can be seen in Figure 13. The image is from the center of a sample of Rene 80 that has been bonded at 1214°C for 3 hours and the red boxes overlaid on the image show where the EDS area scans were taken. In Figure 13 the bondline is the edge of the box denoted 1 and is shown as a blue line. The width of the areas used to acquire the weight percent of zinc varied between specimens. For this specimen, each of the areas was 10 microns wide. For specimens where the interlayer diffused faster, the widths of the areas were increased to reduce the amount of time taken to collect the data for the sample. The distance associated with each area scan was defined as the distance from the bondline to the center of the area scan from which the data was taken.

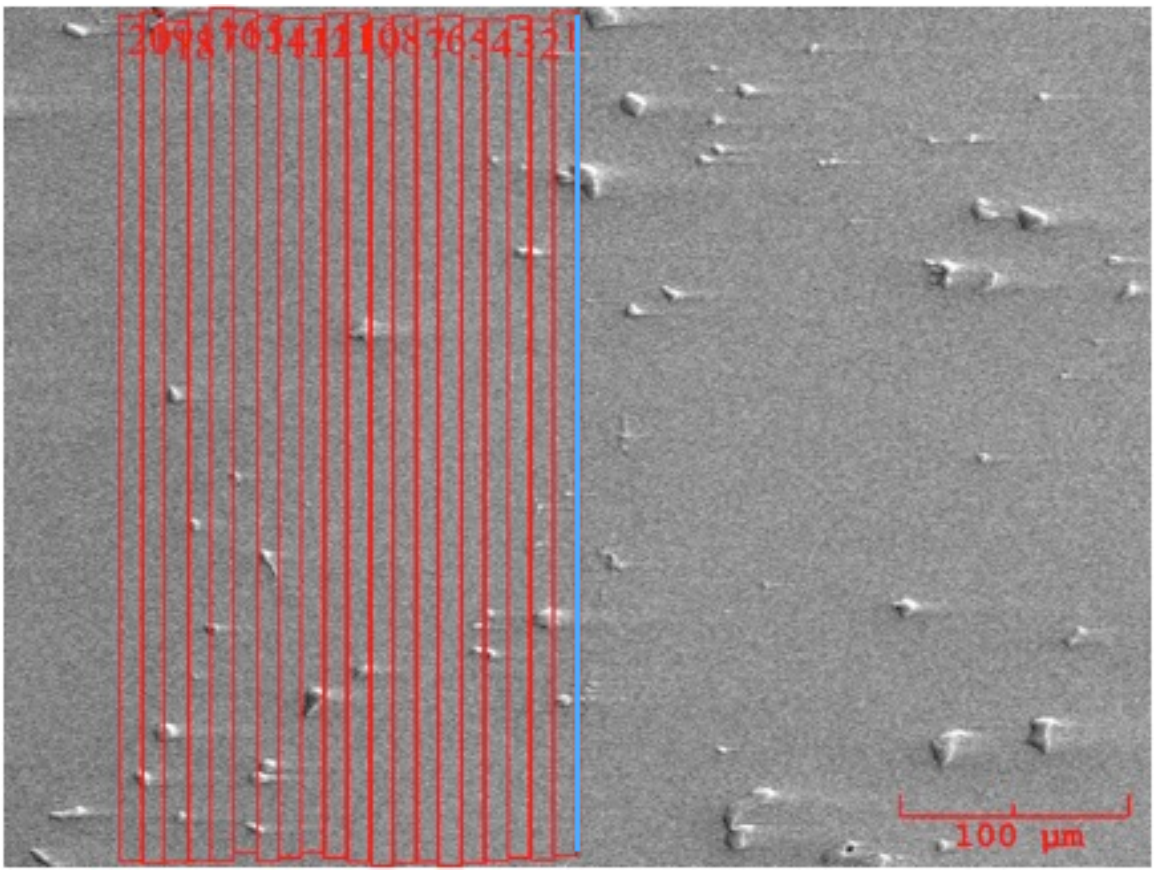

Figure 13 Area scan of Rene 80 bonded at 1214°C for 3 hours

The diffusion coefficient for each sample was calculated using Equation 1 [42]. This equation defines the diffusion of a thin film into a semi-infinite sink.

$$C(x,t) = \frac{\beta}{2\sqrt{\pi D^* t}} \exp\left(\frac{-x^2}{4D^* t}\right) \tag{1}$$

C(x,t) is the concentration of the diffusing atoms in the parent material in weight percent, β is the number of atoms per unit area present in the thin foil at x=0 in atoms/μm^2, D* is the diffusion coefficient in μm^2/min, t is the time that the diffusion is allowed to occur in minutes, and x is the distance into the parent

material that the material has traveled in μm. For a sample where a thin film is diffusing into a semi-infinite solid via bulk diffusion, the diffusion coefficient may decrease as the system is held at the bonding temperature for longer periods of time [42, 43]. This occurs because when the diffusion coefficient is not composition independent [43].

To determine the diffusion coefficient, the natural log of the concentration versus the distance squared is to be plotted. Then, finding the best-fit straight-line slope of this graph the diffusion coefficient can easily be found. The slope of this best fit trend-line is defined in Equation 2, where m is the slope of the trend-line, which can be rearranged to Equation 3 to determine the diffusion coefficient of the sample.

$$m = \frac{-1}{4D^{*}t} \tag{2}$$

$$D^{*} = \frac{-1}{4mt} \tag{3}$$

Table 2 shows the data from the specimen of Rene 80 bonded at 1214°C for 3 hours. The table shows the zinc concentration values with their respective distances along with the square of the distance values and the natural log of the concentration values that are needed to determine the diffusion coefficient. Figure 14 shows a graph of the values in Table 2 with the trend line and best-fit equation displayed. All of the data from the diffusion testing can be found in the appendix.

Table 2 Distance from Bondline to Area Analyzed with Distance Squared Values and Natural Log of Weight Percent for Rene 80 Bonded at 1214°C for 3 Hours

Distance from Center (μm)	Weight percent zinc (%)	x^2	Ln wt%
5	6.789	25	1.915
15	6.972	225	1.942
25	6.214	625	1.827
35	5.591	1225	1.721
45	5.328	2025	1.673
55	4.709	3025	1.549
65	4.144	4225	1.422
75	3.398	5625	1.223
85	2.699	7225	0.993
95	2.081	9025	0.733
105	1.242	11025	0.217
115	0.626	13225	-0.468
125	0.576	15625	-0.552
135	0.467	18225	-0.761
145	0.193	21025	-1.645
155	0.167	24025	-1.789

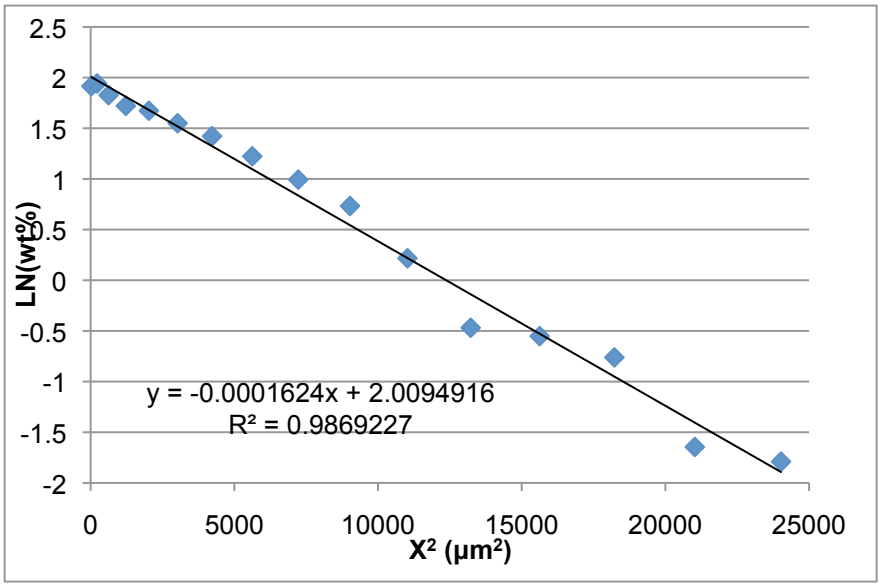

Figure 14 The Natural Log of the Weight Percent vs Distance from the Bondline Squared for Rene 80 Bonded at 1214°C for 3 Hours

In this manner, the diffusion coefficients for each of the diffusion-bonded samples were calculated. Table 3 shows the diffusion coefficient, the R^2 values

for the trendline that was used to determine the diffusion coefficient for each of the samples, and the length of the bond. A schematic of the center of the bond and the edge of the bond can be seen in Figure 15. The empty cells in the table represent samples where the diffusion coefficient could not be determined. This is because either the trendline had a R^2 value that fell below 0.5 or the first three area scans taken all contained zinc weight percents below 0.5%.

Table 3 Diffusion Coefficients, R^2 Values, and Bond Lengths for all Collected Samples

Material	Temp	Time	Center		End		Bond Length
	(°C)	(min)	D (μm^2/min)	R^2	D (μm^2/min)	R^2	(mm)
APMT	700	30	6.0386	0.83	4.0954	0.9919	0
APMT	1155	180	70.146	0.7575	-	-	0
APMT	1155	1200	-	-	-	-	0
APMT	1214	60	299.76	0.8582	192.0122	0.9086	25.46
APMT	1214	180	-	-	-	-	3.753
APMT	1214	300	112.61	0.8923	-	-	18.146
APMT	1214	600	-	-	-	-	23.082
APMT	1214	1200	-	-	-	-	16.537
CM247	700	30	1.2342	0.6537	0.8994	0.9707	0
CM247	1155	180	1.7983	0.9153	-	-	0
CM247	1155	1200	-	-	-	-	0
CM247	1214	60	3.7369	0.9784	9.284	0.9688	11.37
CM247	1214	180	5.7203	0.9211	3.8346	0.9111	11.69
CM247	1214	300	3.7069	0.8994	3.7487	0.9622	9.67
CM247	1214	600	3.8191	0.8887	-	-	4.39
CM247	1214	1200	0.4974	0.8414	-	-	9.36
Rene80	1155	1200	2.4713	0.8615	-	-	0
Rene80	1214	60	11.973	0.9668	8.7278	0.9945	9.73
Rene80	1214	180	8.5523	0.9869	9.2654	0.9845	9.04
Rene80	1214	300	6.688	0.9448	5.7195	0.9358	6.408
Rene80	1214	600	3.4722	0.9437	1.3569	0.7901	11.78
Rene80	1214	1200	3.1855	0.8532	0.3344	0.5854	7.411

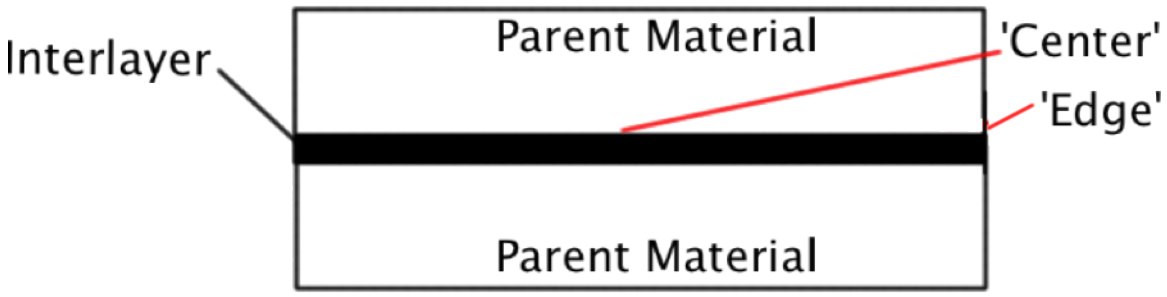

Figure 15 Schematic Showing Locations of ‘Center’ and ‘Edge’

The mass of zinc remaining in the sample was calculated to verify the evaporation of the zinc interlayer. The zinc interlayer is 25 μm thick and it can be assumed that the interlayer is diffusing equally in both directions of the joint. Therefore the zinc starts as a 12.5 μm wide strip the area of the bond and diffuses into the parent material. By assuming that the density of the parent material with the zinc diffused in it is equal to the density of the original parent material, the mass of the volume that the EDS was performed on can be found. Multiplying the weight percent of zinc by the mass of the material in the region and adding the mass from each of the regions can approximate the mass of the diffused zinc. The mass of the zinc diffused into the samples is shown in Table 4.

Table 4. Approximate Mass of Zinc Diffused into Bonded Samples

Material	Temp	Time	Mass of Zinc at Center	Mass of Zinc at End	Initial Mass of Zinc Before Diffusion
	(°C)	(min)	(g)	(g)	(g)
APMT	700	30	7.9657E-09	5.4163E-09	3.1238E-08
APMT	1155	180	6.5698E-09	1.2941E-10	3.1238E-08
APMT	1155	1200	1.8651E-09	1.2548E-09	3.1238E-08
APMT	1214	60	1.1893E-08	1.0789E-08	3.1238E-08
APMT	1214	180	1.1025E-09	9.2365E-10	3.1238E-08
APMT	1214	300	1.9048E-08	2.8566E-09	3.1238E-08
APMT	1214	600	5.2945E-09	2.4874E-09	3.1238E-08
APMT	1214	1200	1.6291E-09	1.1571E-09	3.1238E-08
CM247	700	30	5.0992E-09	7.4857E-09	3.1238E-08
CM247	1155	180	1.5773E-08	7.7350E-12	3.1238E-08
CM247	1155	1200	5.2955E-11	7.0210E-11	3.1238E-08
CM247	1214	60	6.4233E-09	6.4025E-09	3.1238E-08
CM247	1214	180	7.8070E-09	3.4117E-09	3.1238E-08
CM247	1214	300	7.8549E-09	3.6203E-09	3.1238E-08
CM247	1214	600	1.1777E-08	1.2852E-10	3.1238E-08
CM247	1214	1200	4.3280E-09	7.7053E-11	3.1238E-08
Rene80	1155	1200	1.2430E-08	1.6940E-10	3.1238E-08
Rene80	1214	60	1.3204E-08	9.2490E-09	3.1238E-08
Rene80	1214	180	1.4288E-08	1.3652E-08	3.1238E-08
Rene80	1214	300	1.0414E-08	7.8728E-09	3.1238E-08
Rene80	1214	600	4.8888E-09	1.2942E-09	3.1238E-08
Rene80	1214	1200	5.5549E-09	2.5735E-09	3.1238E-08

Table 5 shows the centerline composition of each of the bonded specimens (data taken at the ‘Center’ position of each joint).

Table 5. Centerline Composition of Each Joint (wt% Zn)

Material	Temp (°C)	Time (min)	Center Composition (wt%)
APMT	700	30	16.2
APMT	1214	60	2.6
APMT	1214	300	1.9
CM247LC	700	30	16.7
CM247LC	1214	60	6.9
CM247LC	1214	180	4.1
CM247LC	1214	300	3.5
CM247LC	1214	600	3.7
CM247LC	1214	1200	2.1
Rene 80	1214	60	8.1
Rene 80	1214	180	6.8
Rene 80	1214	300	4.8
Rene 80	1214	600	2.7
Rene 80	1214	1200	1.4

Diffusion Data Analysis

For the APMT samples, the diffusion coefficient at the center of the samples bonded at 1214°C started at 299.76 μm^2/min when bonded for 1 hour and decreased down to 112.61 μm^2/min when bonded for 5 hours. At the times longer than 5 hours, the zinc diffused to a point at which the diffusion coefficient could no longer be determined. The diffusion coefficient for the sample bonded at 1155°C for 3 hours is less than the diffusion coefficient of the sample bonded for the same time at 1214°C. This decrease in diffusion coefficient for the same bonding time but lower bonding temperature is expected as the atoms have less free energy. The diffusion coefficients that could be determined for the data taken at the ends of the samples are less than the diffusion coefficients of those under the same bonding time and temperature of the data taken at the center of the bond.

Similarly, it was found in the Rene 80 samples that the highest diffusion coefficient for a bonding temperature of 1214°C is 11.97 μm^2/min and decreases to 3.18 μm^2/min as the time that the sample is held at the bonding temperature increased from 1 hour to 20 hours. The sample of Rene 80 bonded at 1155°C for 20 hours has a lower diffusion coefficient than that of the sample bonded for 20 hours at 1214°C as is expected as described above. Even though the diffusion coefficients of the Rene 80 at the center decrease as the time increases, the diffusion coefficient at the end of the bond at a bonding time of 3 hours is unexpectedly greater than the diffusion coefficient at the end of the sample

bonded for 1 hour. Aside from the end of the sample bonded at 1214°C for 3 hours the diffusion coefficients behaved as expected, decreasing as the bonding time increased and as the bonding temperature decreased.

The diffusion coefficients for the CM247LC do not follow the expected trend of decreasing values with the increasing time at bonding temperature. At the center of the CM247LC samples, for example, the diffusion coefficient for the sample that was bonded at 1214°C for 1 hour is 3.73 μm^2/min and is less than the diffusion coefficient for the sample bonded at the same temperature for 3 hours which is 5.72 μm^2/min. Interestingly, for the CM247LC the diffusion coefficients at the center of the samples are very close to each other for the samples at 1 hour, 5 hours and 10 hours when it should be decreasing. The diffusion coefficient at the edge of the bond for the sample bonded at 1214°C for 1 hour is 8.12 μm^2/min and decreases to 3.83 μm^2/min when bonded for a time of 3 hours. The diffusion coefficients for the CM247LC samples do not agree with the expected trend nor do they follow any noticeable trend additionally no noticeable changes in material structure or composition were observed that could account for this behavior.

Several observations can be made about the data in Tables 3-5. First, the diffusivity of Zn in both APMT and CM 247 is quite similar at 700°C. Diffusivity in the APMT does appear to be slightly higher (~4 μm^2/min vs ~2 μm^2/min), but the midline composition after 30 minutes at this temperature is quite similar. At 1214°C, the situation is very different. Because only about 15 wt% Zn remained at the midline after the low temperature hold, the absolute difference in

compositions between the APMT, CM247 and Rene 80 at 1214°C is relatively small. However, the calculated diffusivity of Zn in APMT is approximately 20 times higher than in CM 247 or Rene 80 (~120 μm^2/min vs ~8 μm^2/min) at 1214°C. Equation 4 is the standard expression for the diffusivity in terms of the diffusion coefficient, Do, and the activation energy for diffusion, Q, where R is the ideal gas constant and T is the absolute temperature:

$$D^* = D_0 \exp(-QRT) \tag{4}$$

If Do and Q are assumed to be independent of temperature and composition for each material system and the approximate ratio of the diffusivities calculated above is substituted into Equation 5 for APMT and CM247, the difference in activation energies for diffusion of Zn through the two alloys can be estimated. This calculation yields:

$$Q_{CM\ 247LC} - Q_{APMT} \cong -54\ {}^{kJ}/_{kmol} \tag{5}$$

For reference, this value is similar in magnitude and sign to the difference in activation energies for the diffusion of copper in pure nickel (258 kJ/kmol) and pure iron (295 kJ/kmol) [44].

For each of the samples it was found that the amount of zinc that had diffused into the parent material was greater at the center than at the end of the sample with the exception of the CM247LC sample bonded at 1155°C for 20

hours, however, this specimen did not create a bonded part. By observing that the amount of zinc is greater at the center than at the edge of the bond it can be determined that the zinc was not just diffusing into the parent material but also out of the edges of the material as is expected for evaporative metal bonding.

Theoretical calculations on the diffusion of various impurities in different materials have been performed by Zacherl. These calculations included the diffusion of zinc in pure nickel as a function of temperature. From these theoretical calculations the diffusion coefficient of zinc in pure nickel at 1200°C can be found to be approximately 3 μm^2/min [45]. This theoretical value helps to validate the diffusion coefficients determined for the zinc in the nickel alloys CM247LC and Rene 80 in the current study. Additionally, the diffusion coefficients for the Rene 80 appear to be approaching this theoretical value. Furthermore, even though the diffusion coefficients for the CM247LC do not appear to follow any trend they are, for the most part, very close to this theoretical value.

Finite Element Modeling Data

The thermal expansion data for all materials was collected using a Shimadzu TMA60, which automatically corrects the thermal expansion measurement with an alumina reference sample. Each sample was heated in an argon atmosphere at 100°C increments and held for 15 minutes at each temperature up to 1200°C. The coefficient of thermal expansion for each of the samples was calculated using Equation 6 where α is the coefficient of thermal

expansion in m/m°C, l is the initial length of the specimen in m, Δl is the change in length of the specimen in m, and ΔT is the change in temperature from the initial temperature in °C.

$$\alpha = \frac{\Delta l}{l}\frac{1}{\Delta T} \tag{6}$$

The linear coefficient of thermal expansion used in the finite element model was found by averaging the coefficient of thermal expansion for each data point within 2°C of the holding temperature and averaging these values across the 4 tests done for each sample. The thermal expansion values found from the TMA data for the Rene 80 and APMT are consistent with those reported in literature [35, 47]. CM247LC is a similar alloy to Rene 80 and so the thermal expansion of the two alloys should be similar. Table 6 shows the coefficients of thermal expansion for each of the parent materials at each temperature as well as the standard deviation of the data. Table 7 shows the coefficients of thermal expansion for the steel hemispheres. The thermal expansion data for the molybdenum was also measured. However, when comparing this data to published data the experimentally found values were over twice the published data. Therefore, the coefficient of thermal expansion for molybdenum was taken to be a constant 6E+-06 m/m°C as published [46].

Table 6. Coefficients of Thermal Expansion for Parent Materials

	Rene 80		CM247LC		APMT	
Temperature	CTE (m/m°C)	St Dev	CTE (m/m°C)	St Dev	CTE (m/m°C)	St Dev
100	1.30E-05	8.85E-08	1.23E-05	3.38E-08	1.42E-05	6.02E-08
200	1.42E-05	6.58E-08	1.36E-05	6.53E-08	1.46E-05	1.10E-07
300	1.52E-05	4.09E-08	1.48E-05	3.75E-08	1.58E-05	5.89E-08
400	1.59E-05	2.31E-08	1.56E-05	2.23E-08	1.66E-05	2.80E-08
500	1.64E-05	1.75E-08	1.62E-05	1.40E-08	1.69E-05	2.24E-08
600	1.68E-05	1.21E-08	1.67E-05	1.01E-08	1.70E-05	1.15E-08
700	1.72E-05	7.77E-09	1.71E-05	6.99E-09	1.71E-05	4.84E-09
800	1.75E-05	4.41E-09	1.74E-05	5.57E-09	1.73E-05	5.02E-09
900	1.80E-05	3.72E-09	1.77E-05	3.66E-09	1.76E-05	3.13E-09
1000	1.86E-05	2.98E-09	1.79E-05	1.32E-08	1.78E-05	8.13E-09
1100	1.96E-05	2.25E-08	1.75E-05	1.95E-08	1.78E-05	1.06E-08
1200	2.06E-05	4.69E-10	1.74E-05	1.28E-09	1.80E-05	8.47E-09

Table 7. Coefficient of Thermal Expansion for Steel

	Steel	
Temperature	CTE (m/m°C)	St Dev
100	1.14E-05	2.24E-07
200	1.51E-05	1.50E-07
300	1.75E-05	8.31E-08
400	1.84E-05	4.56E-08
500	1.87E-05	2.17E-08
600	1.87E-05	1.16E-08
700	1.85E-05	6.62E-09
800	1.69E-05	1.29E-08
900	1.88E-05	1.20E-08
1000	1.94E-05	1.15E-08
1100	1.86E-05	3.02E-08
1200	1.72E-05	4.69E-08

The finite element analysis was performed using ANSYS Workbench 14.0. The modulus of elasticity and Poisson's ratio for each material were assumed constant for the test and were taken from literature and shown in Table 8 [35, 46-

50]. The coefficients of thermal expansion used were determined via the TMA analysis. From the thermal expansion values, the foil interlayer was left out of the model as the materials being bonded thermally expand over 4 times the thickness of the foil.

Table 8. Modulus of Elasticity and Poisson's Ratio Used in Finite Element Model [35, 46-50]

Material	Poisson's Ratio	Modulus of Elasticity (GPa)
APMT	0.3	220
CM247LC	0.4	152
Rene 80	0.3	210
Steel	0.3	210
Molybdenum	0.38	330

The mesh sizing of the models was determined from a mesh refinement convergence analysis. The model with the initial representative values was meshed with a fine relevance center, high smoothing, fine span angle center, and the midside nodes were kept. The fine relevance center was chosen to decrease the program chosen default size of the elements in the mesh. The high smoothing and the fine span angle center were chosen so that the program would improve the mesh around the curves of the model. Having the midside nodes in the model enables an extra node at the center of each element edge, which increases the order of the elements from linear to quadratic, which should increase the accuracy of the model. The maximum allowable size of the edge of the elements were then varied and the maximum von Mises stress at the bondface was measured until it no longer changed. Table 9 shows the element size, number of nodes in the model corresponding to the given element size, the

maximum stress at the bondface, and the percentage difference of the current element size from the next largest element size. Figure 16 shows a graph of the maximum stress at the bondface vs. the number of nodes in the model.

Table 9. Results from Mesh Refinement

Element Size (mm)	Number of Nodes	Max Stress at Bondface (Pa)	% difference
4	9993	2.80E+08	
3	25807	2.77E+08	-1.06
2.5	47248	2.76E+08	-0.36
2	72673	2.76E+08	0.01
1.75	113603	2.76E+08	-0.14
1.5	155561	2.76E+08	0.04

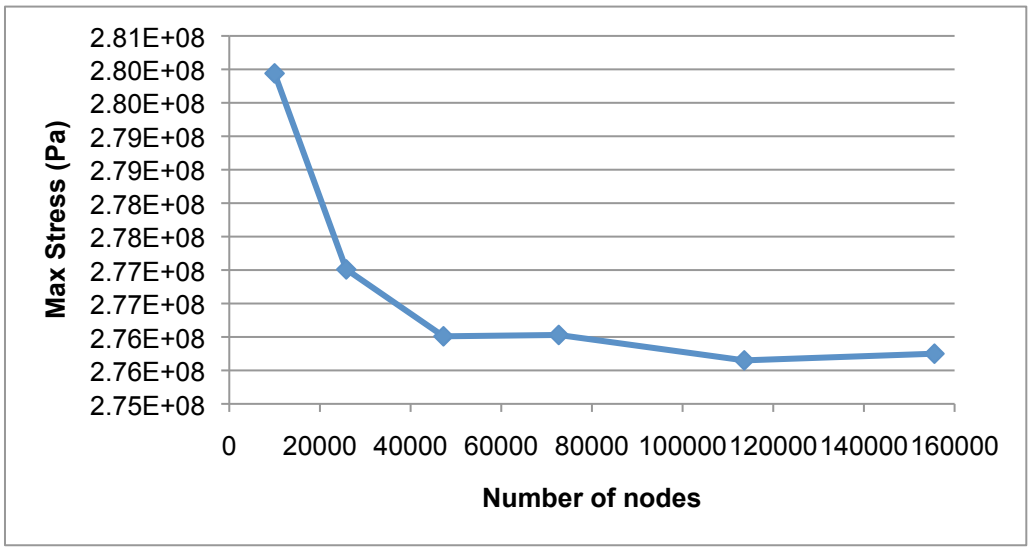

Figure 16. Maximum Stress at the Bondface vs. the Number of Nodes in the Model

From the mesh refinement study it was concluded that an element size of 2.5 mm creates a mesh that is fine enough. Figures 17 a&b show the final meshed models. Figure 17a shows the meshed model for the CM247LC and the Rene 80 bonding while Figure 17b is the meshed model for the APMT.

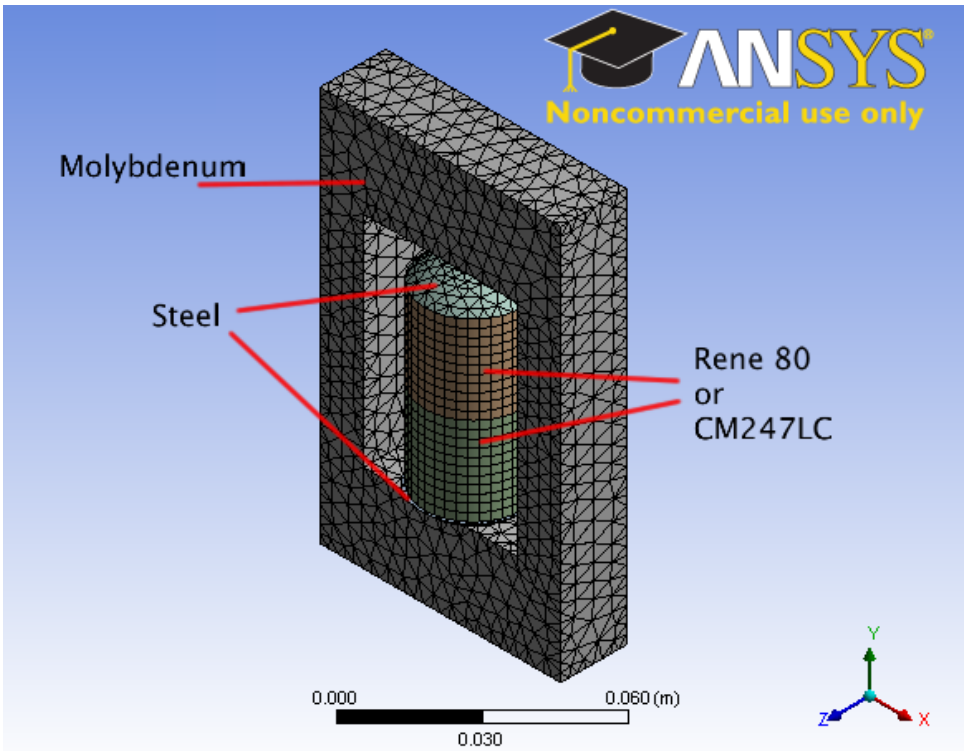

a)

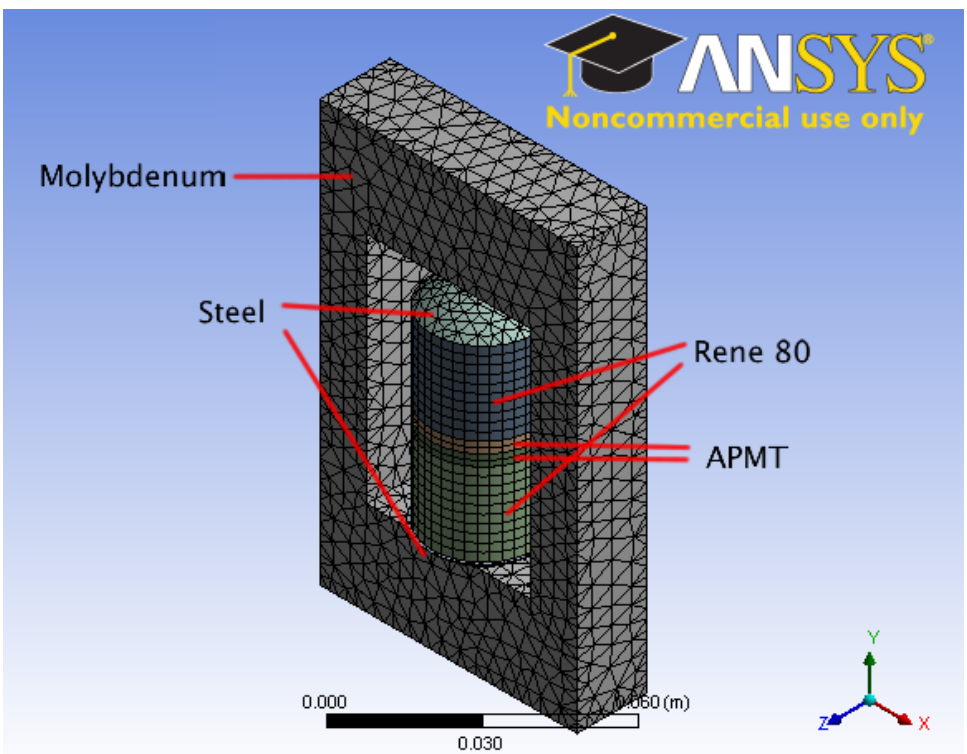

b)

Figure 17 a) Meshed Model Used for Simulation of CM247LC and Rene 80 Bonding b) Meshed Model Used for Simulation of APMT Bonding

The model was run in 12 steps taking data starting at an ambient temperature of 22°C then at 100°C and at every subsequent 100°C increment all the way up to 1200°C. By performing the analysis in steps, transformation in the stress state can be observed. The stresses of most interest in this study are those at the bondface as those must be matched in future models of more complicated structures to assure that the same conditions are applied. By matching the stress state at the bonding temperature for a complex geometry with that of the simple bonding setup, the bond of the complex geometry can be assured. Figure 18 a&b shows the normal and von Mises stress state at 1200°C for the model consisting of just CM247LC being bonded. Figure 19 a&b shows the normal and von Mises stress state at 1200°C for the model consisting of Rene 80 being bonded. Figure 20 a&b shows the normal and von Mises stress at 1200°C for the model where Rene 80 was used to hold the APMT samples in place. Figure 21 a&b shows the normal and von Mises stress at 1200°C for the model where Rene 80 was used to hold the APMT samples in place at the APMT Rene 80 interface. Table 10 shows the minimum and maximum normal stress values at the bondface for each of the models at each temperature found from the finite element model. Table 11 shows the minimum and maximum von Mises stress values at the bondface for each of the models at each temperature found from the finite element model.

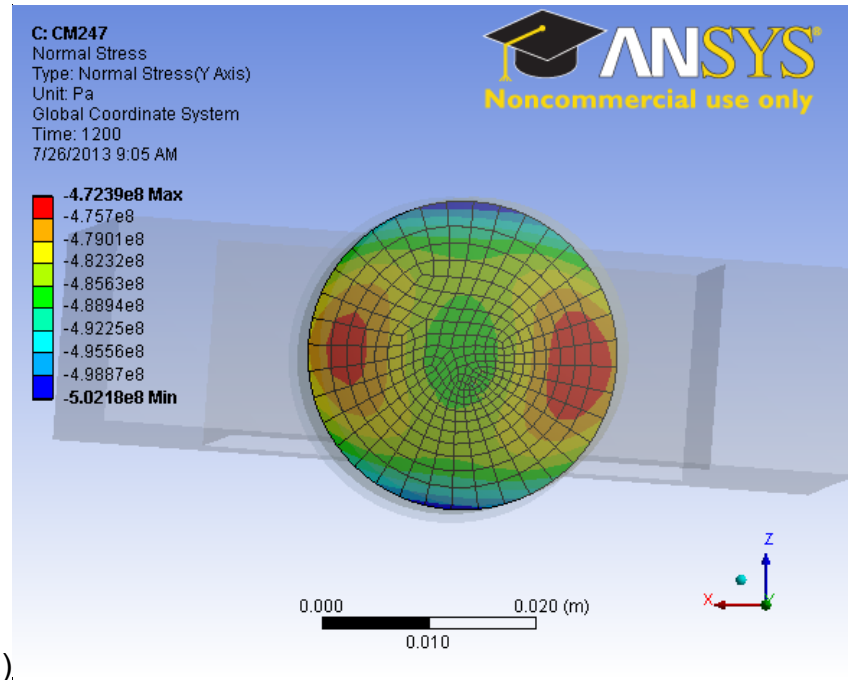

a)

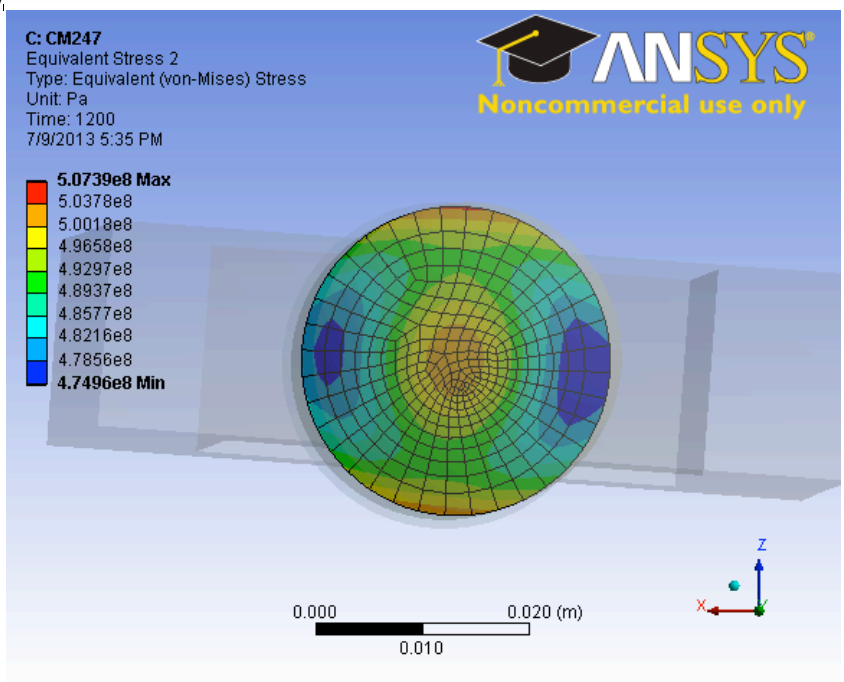

b)

Figure 18. a) Normal Stress Distribution and b) von Mises Stress Distribution at the Bondface at 1200°C for CM247LC

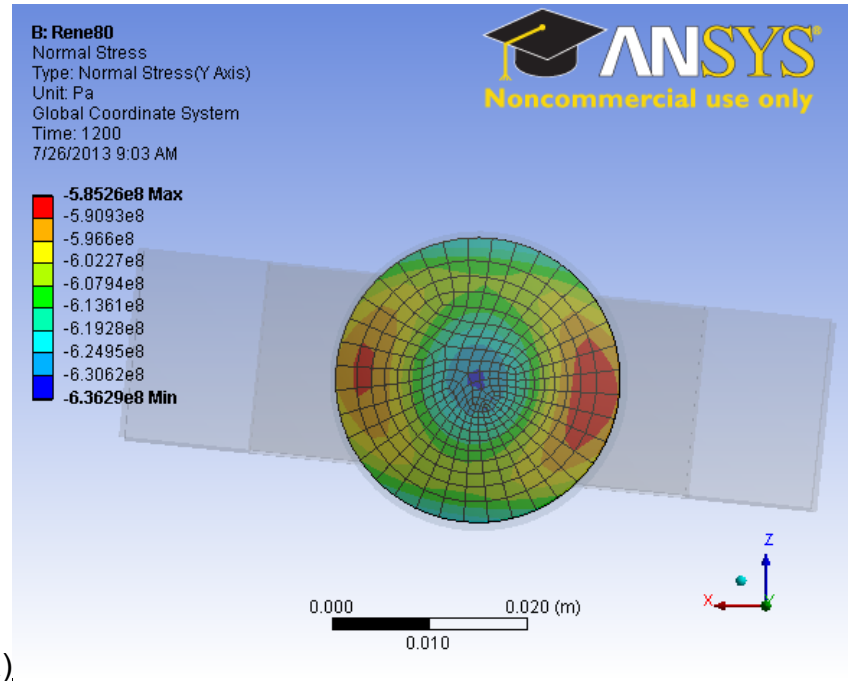

a)

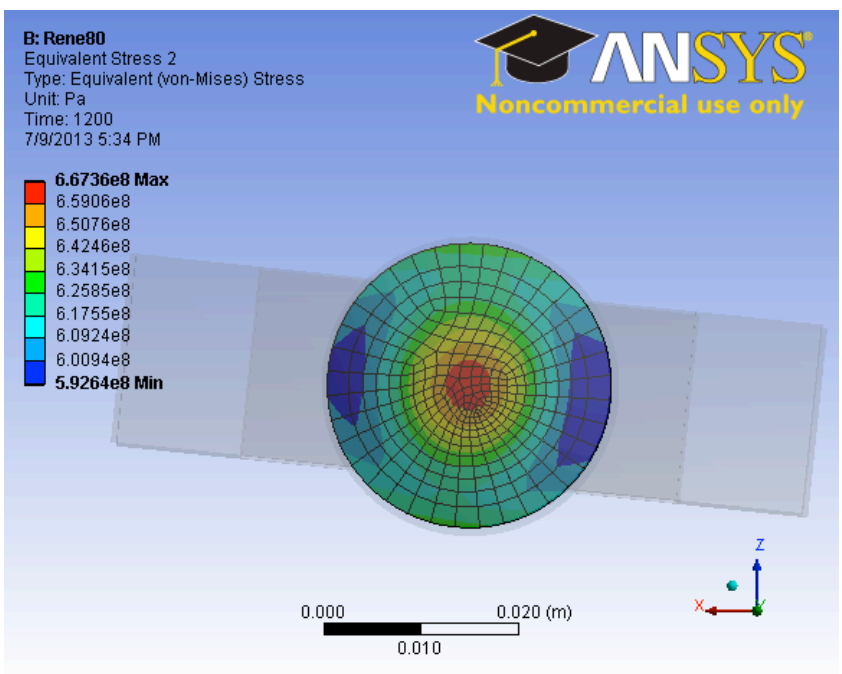

b)

Figure 19. a) Normal Stress Distribution and b) von Mises Stress Distribution at the Bondface at 1200°C for Rene 80

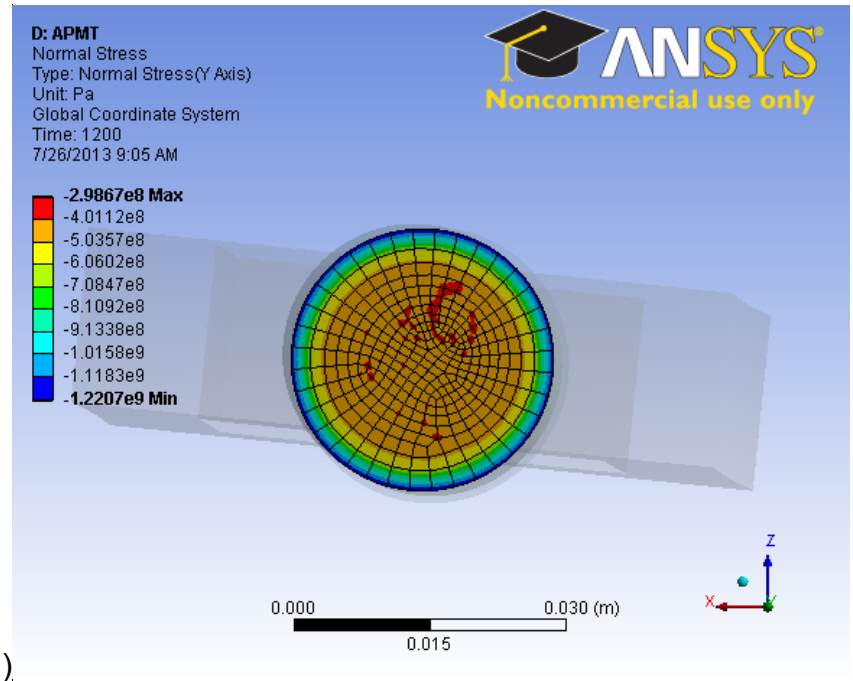

a)

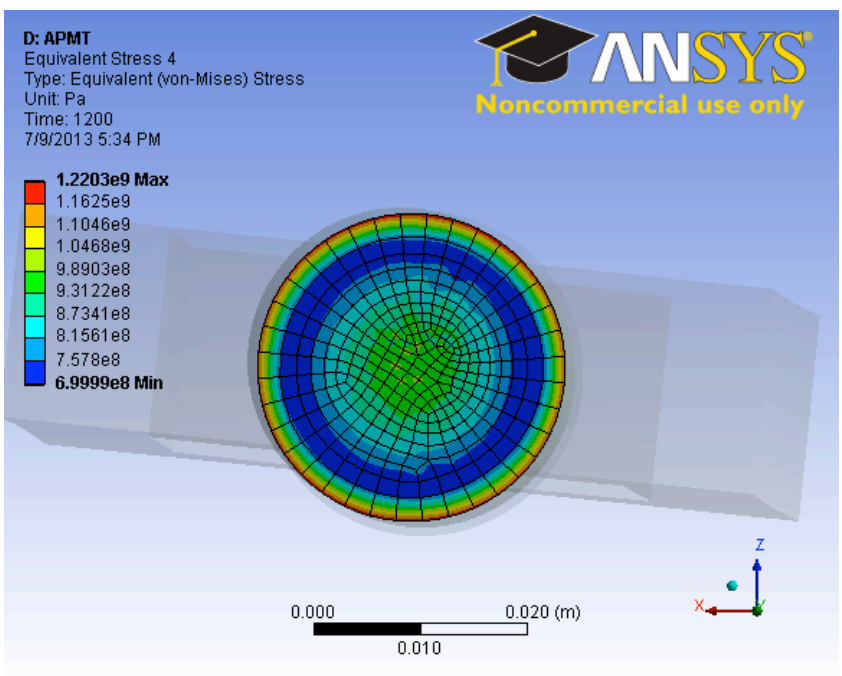

b)

Figure 20. a) Normal Stress Distribution and b) von Mises Stress Distribution at the Bondface at 1200°C for APMT

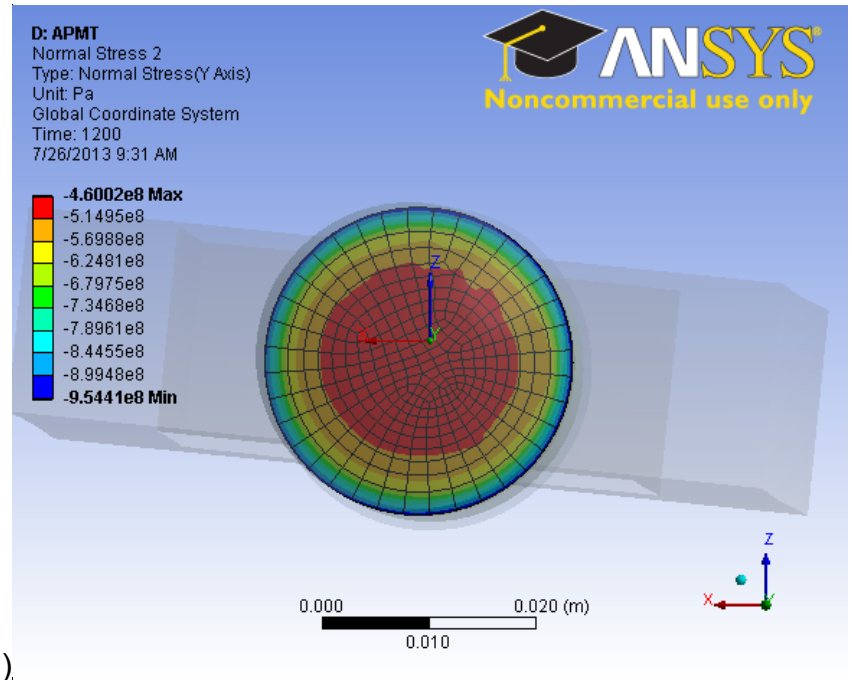

a)

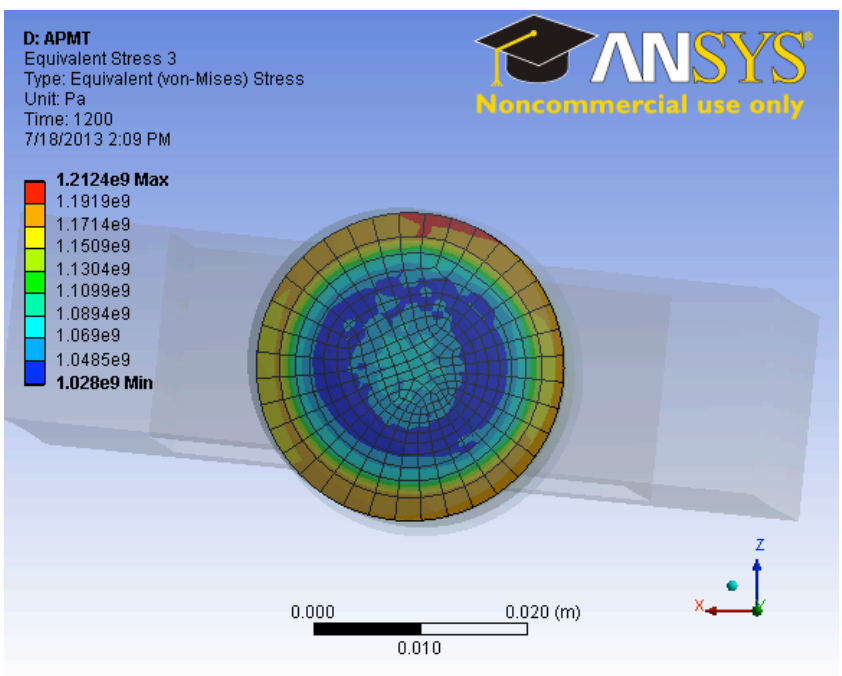

b)

Figure 21. a) Normal Stress Distribution and b) von Mises Stress Distribution at the Interface of APMT and Rene 80 for the Bonding of APMT at 1200°C

Table 10. Minimum and Maximum Normal Stresses from Finite Element Models

	Rene 80		CM247LC		APMT	
Temperature (°C)	Minimum (Pa)	Maximum (Pa)	Minimum (Pa)	Maximum (Pa)	Minimum (Pa)	Maximum (Pa)
100	-2.02E+07	-1.86E+07	-1.77E+07	-1.67E+07	-3.56E+07	1.08E+06
200	-5.87E+07	-5.48E+07	-5.38E+07	-5.04E+07	-8.49E+07	-3.96E+07
300	-1.07E+08	-9.94E+07	-1.00E+08	-9.27E+07	-1.56E+08	-6.47E+07
400	-1.56E+08	-1.45E+08	-1.48E+08	-1.37E+08	-2.29E+08	-9.09E+07
500	-2.06E+08	-1.92E+08	-1.96E+08	-1.83E+08	-2.94E+08	-1.42E+08
600	-2.55E+08	-2.38E+08	-2.45E+08	-2.30E+08	-3.50E+08	-1.69E+08
700	-3.05E+08	-2.85E+08	-2.93E+08	-2.75E+08	-4.05E+08	-1.95E+08
800	-3.43E+08	-3.21E+08	-3.29E+08	-3.10E+08	-4.56E+08	-2.21E+08
900	-4.18E+08	-3.91E+08	-3.97E+08	-3.73E+08	-5.35E+08	-2.58E+08
1000	-4.89E+08	-4.56E+08	-4.53E+08	-4.26E+08	-6.37E+08	-2.87E+08
1100	-5.59E+08	-5.23E+08	-4.79E+08	-4.50E+08	-9.34E+08	-2.92E+08
1200	-6.36E+08	-5.85E+08	-5.02E+08	-4.72E+08	-1.22E+09	-2.99E+08

Table 11. Minimum and Maximum von Mises Stresses from Finite Element Models

	Rene 80		CM247LC		APMT	
Temperature (°C)	Minimum (Pa)	Maximum (Pa)	Minimum (Pa)	Maximum (Pa)	Minimum (Pa)	Maximum (Pa)
100	1.88E+07	2.12E+07	1.68E+07	1.83E+07	3.79E+05	2.03E+07
200	5.50E+07	5.89E+07	5.06E+07	5.40E+07	3.62E+07	7.04E+07
300	9.97E+07	1.07E+08	9.31E+07	1.00E+08	5.96E+07	1.23E+08
400	1.46E+08	1.57E+08	1.38E+08	1.48E+08	8.49E+07	1.79E+08
500	1.92E+08	2.06E+08	1.84E+08	1.97E+08	1.25E+08	2.45E+08
600	2.39E+08	2.56E+08	2.31E+08	2.46E+08	1.77E+08	3.19E+08
700	2.86E+08	3.07E+08	2.76E+08	2.94E+08	2.38E+08	4.00E+08
800	3.23E+08	3.54E+08	3.12E+08	3.34E+08	2.86E+08	4.66E+08
900	3.92E+08	4.23E+08	3.74E+08	3.98E+08	3.58E+08	5.70E+08
1000	4.58E+08	4.94E+08	4.27E+08	4.55E+08	4.61E+08	6.93E+08
1100	5.27E+08	5.79E+08	4.51E+08	4.81E+08	5.88E+08	9.37E+08
1200	5.93E+08	6.67E+08	4.75E+08	5.07E+08	7.00E+08	1.22E+09

Finite Element Modeling Data Analysis

To verify the stresses from the finite element model hand calculations were performed. For the hand calculations the model was first simplified to just the molybdenum supports of the jig and bonded in parallel to the sample the same length of the supports as shown in Figure 22.

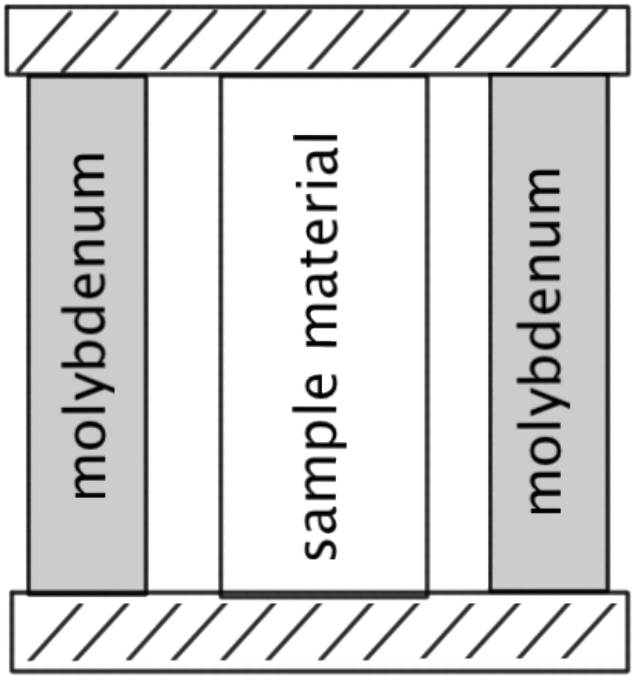

Figure 22. Schematic of Simplified Model Used for Hand Calculations

Next, the coefficient of thermal expansion for each setup was calculated using Equation 7 [51], where α_{total} is the total coefficient of thermal expansion, α_S is the coefficient of thermal expansion of the sample, α_J is the coefficient of thermal expansion of the jig supports, E_S is the modulus of elasticity of the sample, E_J is the modulus of elasticity of the jig supports, V_S is the volume fraction of the sample, and V_J is the volume fraction of the jig supports.

$$\alpha_{total} = \frac{E_S \alpha_S V_S + E_J \alpha_J V_J}{E_S \alpha_s + E_J \alpha_J}$$ Equation 7

The change in length due to thermal loading of each simplified model was then calculated using Equation 8, where ΔL is the change in length, L is the initial length, α is the coefficient of thermal expansion, and ΔT is the change in temperature.

$$\Delta L = L\alpha\Delta T$$ Equation 8

Next, the compressive deformation of each sample was calculated by subtracting the total thermal deformation of the simplified model from the total deformation of the unconstrained sample. This deformation was then changed into the strain of the specimen. Finally, using Hooke's Law and the modulus of elasticity of the sample the stress could be found. These steps are shown in Equations 9-11.

$$\Delta L_{Compressive} = \Delta L_{FreeSample} - \Delta L_{Model}$$ Equation 9

$$\varepsilon = \frac{\Delta L_{Compressive}}{L + \Delta L_{FreeSample}}$$ Equation 10

$$\sigma = E\varepsilon$$ Equation 11

From these calculations the normal stress for the APMT model was calculated to be 1.39E+9 Pa, the stress for the CM247LC model was calculated to be 1.09E+9 Pa, and the stress for the Rene 80 was calculated to be 1.31E+9 Pa. These calculations produce stresses that are 2x the stresses for the CM247LC and Rene 80 model and 1.1x the stress for the APMT model. However, these calculations neglect bending of the top and bottom of the jig, the deformation of the steel hemispheres, the contact between the hemispheres and the jig, as well as the bolt that holds the sample in place. Each of these will increase the deformation of the entire model and as such decrease the total compressive deformation that will reduce the stress at the bondface. Therefore the stress values from the finite element model are determined to be reasonable.

It can be observed that both the maximum and minimum stress at the bondface increase as the temperature increases for each of the models. The increase in stress with the increase of temperature is expected as the materials expand as the temperature increases. All of the materials constrained by the molybdenum jig have larger coefficients of thermal expansion than the molybdenum. This observation is another verification that the model is behaving properly. The most important observation to make of the finite element models is that of how the stress distribution across the bondfaces develops.

For each of the models it can be seen that the stress distribution is not even all the way around the bondface. In each of the models the stress on the bondface at the edge near the vertical supports of the jig is less than the stress at the edge that is farthest from the jig support. It was theorized that the shape of

these stress distributions could be from either the stiffness of the supports of the jig or from the irregular shape of the contact surface between the steel hemispheres and the jig. To determine what was causing the uneven stress distribution the jig was removed from the model of Rene 80 and the steel hemispheres were constrained so as to recreate the contact surface of the jig as well as different contact situations to determine optimal end conditions for a jig for the bonding of complex geometries. The Rene 80 was chosen because it exhibited the largest variation in stress around the perimeter of the bondface.

Boundary conditions for the model tested varied from small circular contact and thin irregular contact surfaces to contact of the full hemisphere. The boundary conditions used and stress distributions for some of these tests can be seen in Figures 23 – 31.

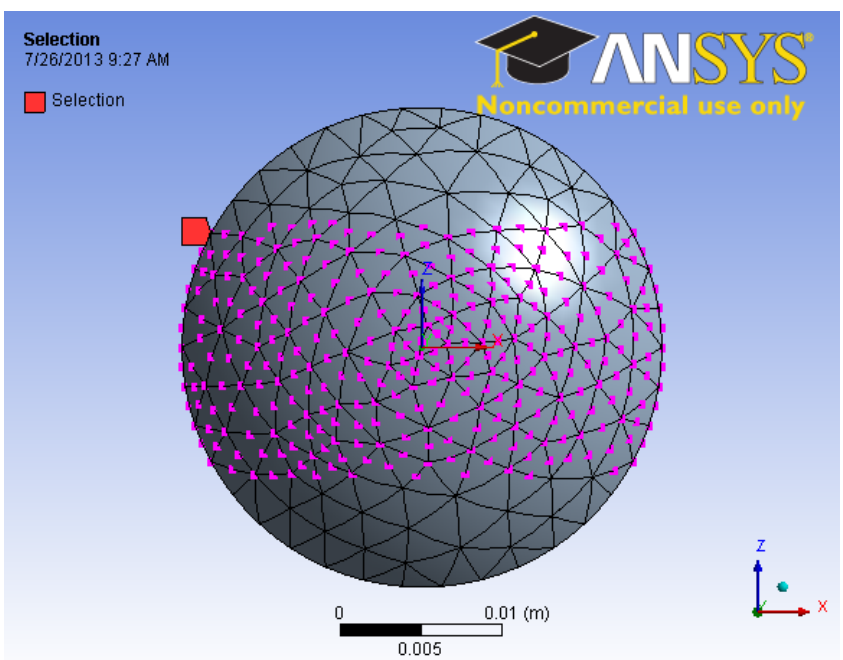

Figure 23. Boundary Conditions C for Rene 80 With Simulated Irregular Jig Contact

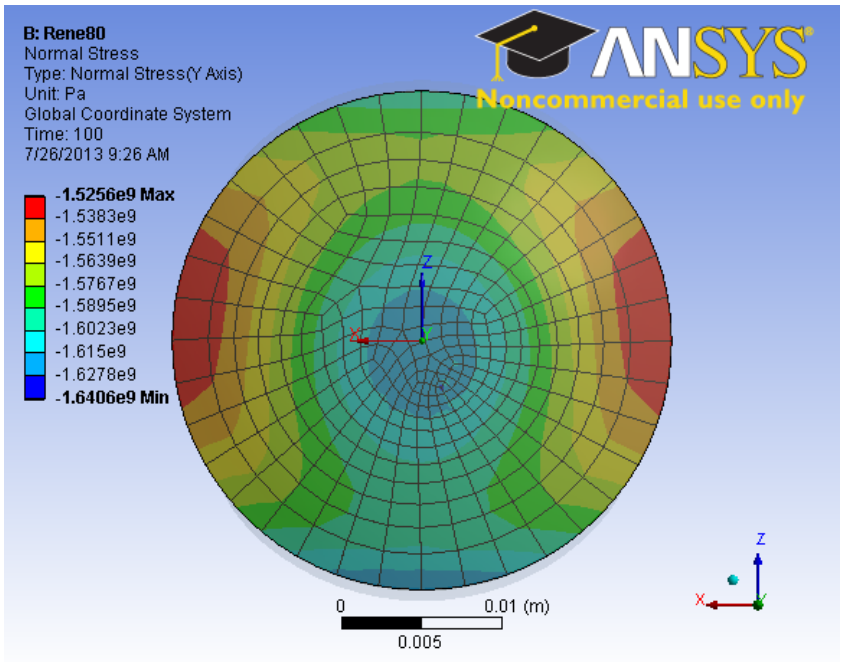

Figure 24. Normal Stress Distribution at the Bondface at 1200°C for Rene 80 With Simulated Irregular Jig Contact

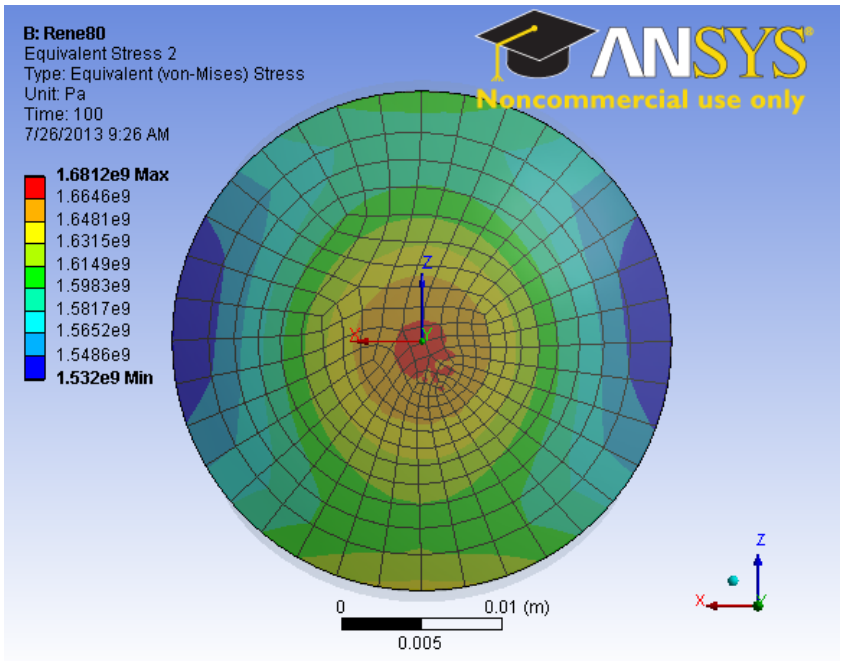

Figure 25. von Mises Stress Distribution at the Bondface at 1200°C for Rene 80 With Simulated Irregular Jig Contact

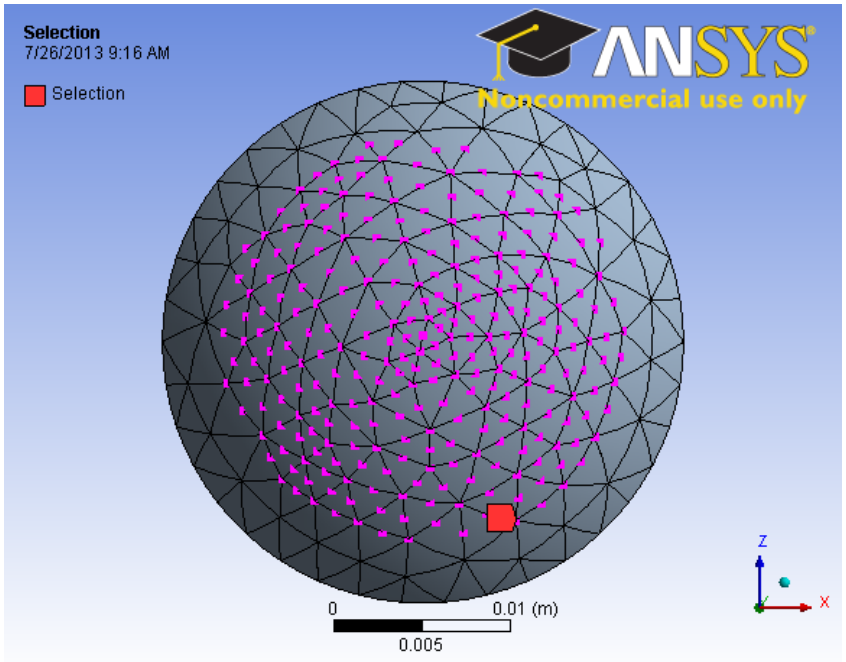

Figure 26. Boundary Conditions for Rene 80 With Simulated Circular Jig Contact

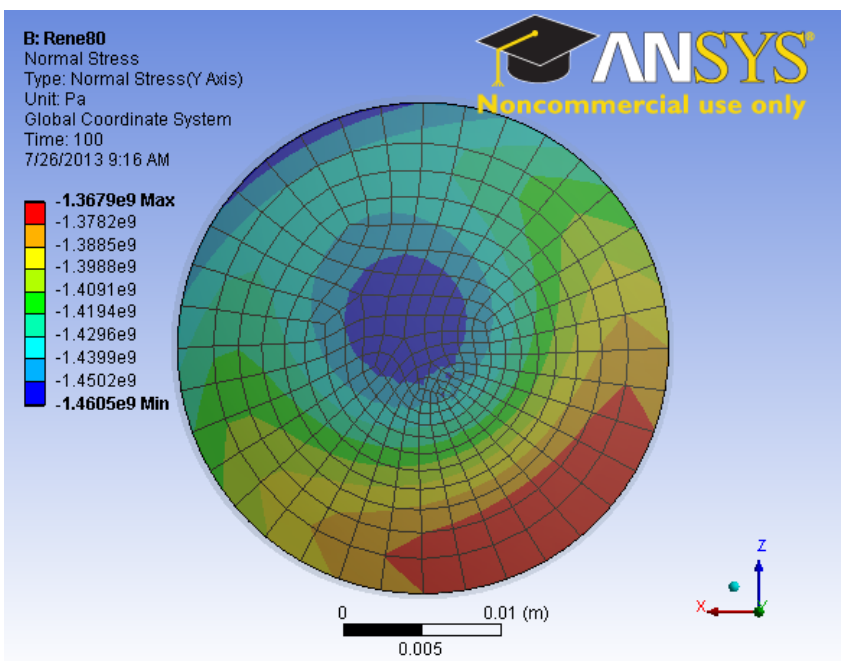

Figure 27. Normal Stress Distribution at the Bondface at 1200°C for Rene 80 With Simulated Circular Jig Contact

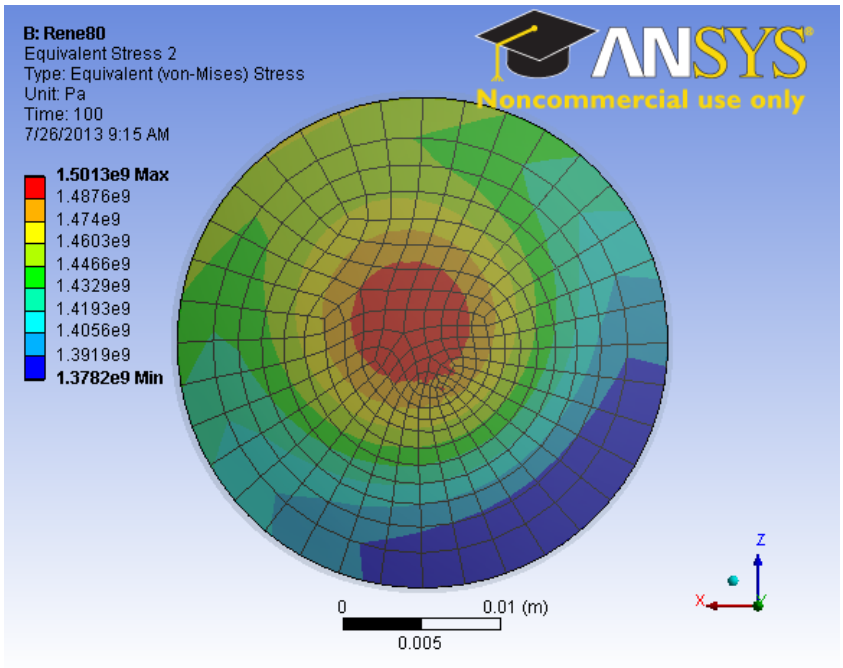

c)

Figure 28. von Mises Stress Distribution at the Bondface at 1200°C for Rene 80 With Simulated Circular Jig Contact

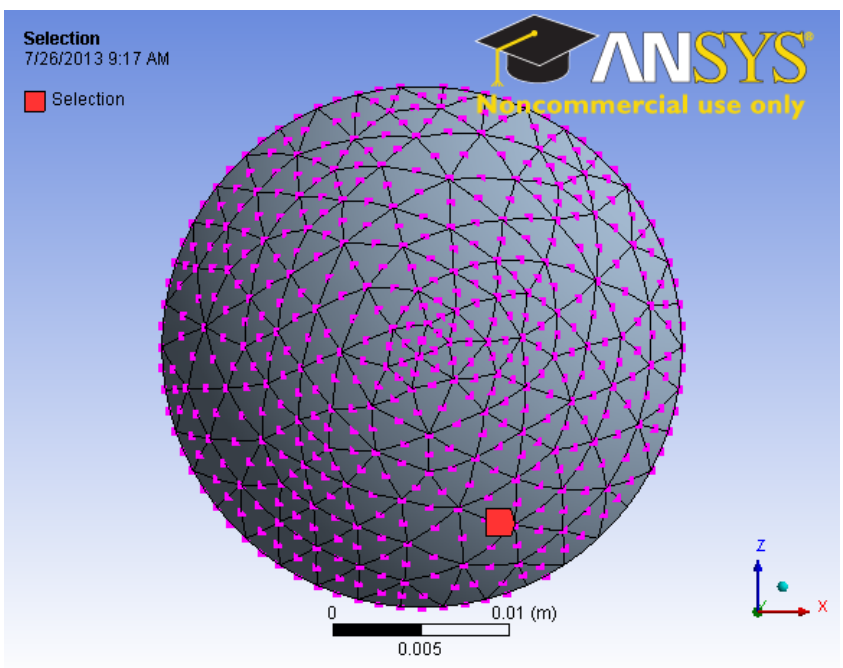

Figure 29. Boundary Conditions for Rene 80 With Fully Supported Hemispheres

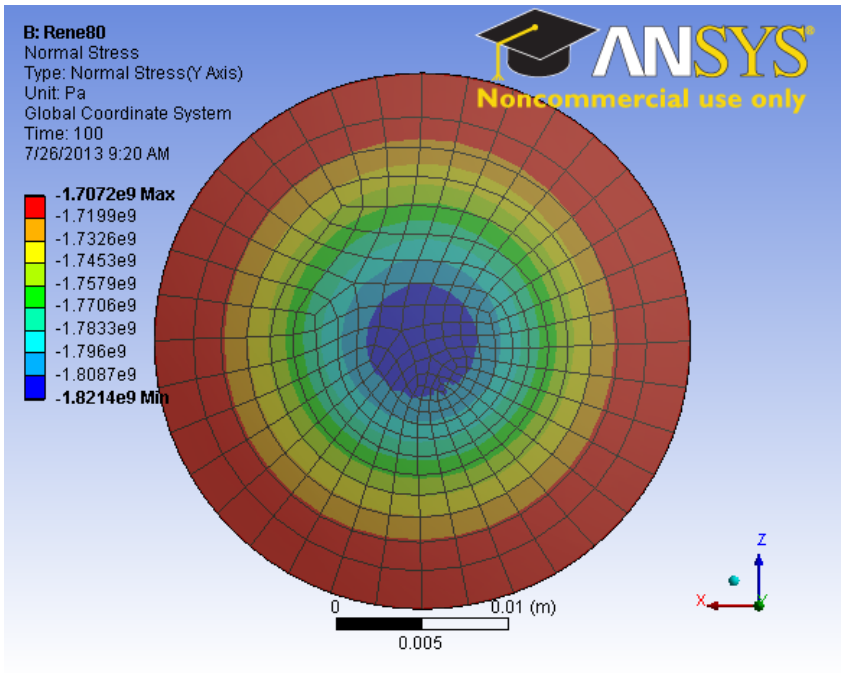

Figure 30. Normal Stress Distribution at the Bondface at 1200°C for Rene 80 With Fully Supported Hemispheres

c)

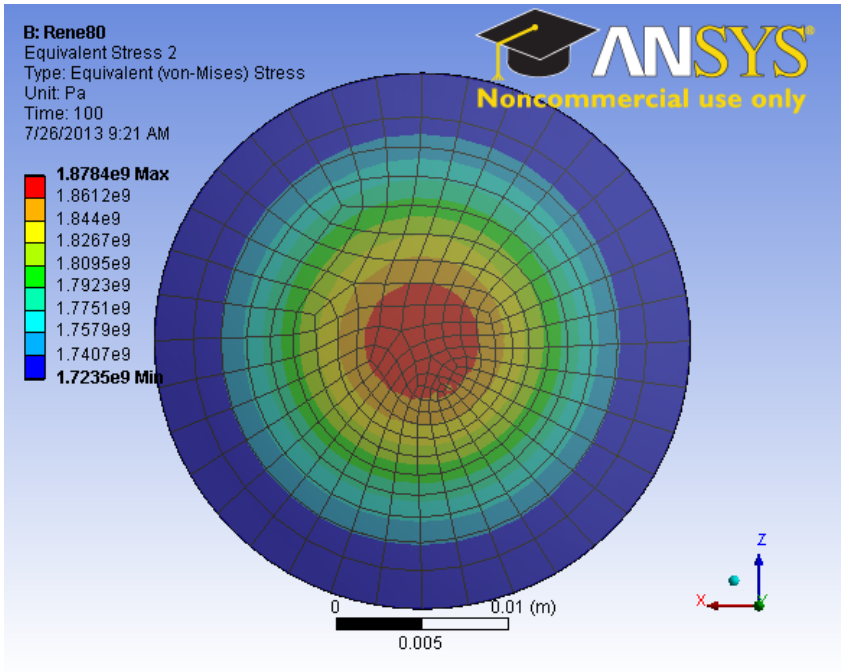

Figure 31. von Mises Stress Distribution at the Bondface at 1200°C for Rene 80 With Fully Supported Hemispheres

Table 12. Maximum Normal and von Mises Stresses from Boundary Conditions Modeling

Geometry of Contact	Maximum Normal Stress (Pa)	Maximum von Mises Stress (Pa)
Irregular Jig	-1.525E+09	1.525E+09
Circular Jig	-1.367E+09	1.367E+09
Fully Supported	-1.707E+09	1.878E+09

For each of these models it can be seen that the maximum stress is greater than that in the models with the jig. This is because the model was constrained such that the top of the samples would expand equal to the theoretical expansion that was found in the verification of the model results and as stated this expansion does not account for many additional deflections that may occur within the complete model. From this analysis of the end conditions it can be seen that the shape of both the normal stress distribution and the von Mises stress distribution in the original model where there is increased stress at the bondface near the jig supports can be attributed to the contact shape of the sample and hemispheres with the jig. A more uniform stress distribution was achieved when a circular contact on the hemisphere was implemented and the most axisymmetric distribution was achieved when the entire hemisphere was constrained.

The room temperature yield strengths for the bonding materials can be seen in Table 13 [32, 47, 50]. For the models simulating CM247LC and Rene 80 the maximum stress values from the model show that neither the CM247LC nor the Rene 80 models achieved a stress at the bondface greater than the parent

material yield strength. This observation agrees with the experimentally bonded specimens where it was observed that none of these samples experienced a measureable amount of yielding during bonding. However, it is expected that the yield strengths of the materials would decrease as the temperature increase. It can be seen that for the cases where CM247LC and Rene 80 are the samples being bonded that the pressure is greatest at the center of the bonding area and decreases to a minimum out to the edge of the bond. This agrees with the previous research performed by Ekrami et al. where they found that bonding Rene 80 to itself created the greatest hardness at the center of the bonding area and the hardness decreased farther from the center [20]. As previously stated, the high hardness at the bond center can be attributed to the high pressure. The similarities between the stress distribution in the current model and with the stress distributions from pervious studies shows that the current models give a reasonable representation of the stresses present at the bonding temperature.

Table 13. Bonding Material Yield Strengths [32, 47, 50]

Material	Yield Strength (MPa)
APMT	540
CM247LC	825
Rene 80	1034

For the model simulating the bonding of the APMT, the maximum stress at the bondface does surpass the yield strength of the APMT so the material at the bondface likely yields to some extent [35]. However, no measureable deformation was observed in the experimental specimens. It can be seen from Figure 20 that the stress is fairly uniform from specimen centerline outward then

the stress decreases to a minimum before increasing to a maximum at the edge of the bond. This bullseye shape distribution of stress seen in the APMT model largely resembles the work reported by Xiaoquin et al. with their work bonding Al_2O_3–TiC to itself using W18Cr4V as a sandwich layer [32]. The previous study reported the residual stresses present surrounding the bond after the bonding of the materials was completed and the sample had returned to room temperature. The residual stresses present at the bonding area arise from the stresses that are present during the bonding of the materials. The pressure that is applied during the bonding of the materials helps to create the contact between the materials. This pressure creates plastic deformation of the materials and areas where the greatest pressure is applied experience the largest plastic deformation. As such the larger the plastic deformation of the material the smaller the residual stresses that will arise at the bonding region [32]. Although in the current study the purpose is to bond two plates of APMT together and not bond a sandwich layer, as in the previous study of Xiaoquin et al., the stress distributions can be determined to be similar because in the current work the APMT did also bond with the Rene 80 that was used to hold it in place. Therefore, the stresses present at the bondface between the APMT plates can be likened to the stress reported at the middle of the W18Cr4V. However, the stress distribution in the current model of APMT has a stress distribution that is the inverse of the stress distribution that the previous study reported. This is because the APMT has a lower modulus of elasticity than the Rene 80, the opposite of the previous study where W18Cr4V has a larger modulus of elasticity

than the Al_2O_3–TiC. Running the model again but changing the material properties around so that the thick plug material has a higher modulus than the plates at the center confirmed this and is shown in Figure 32.

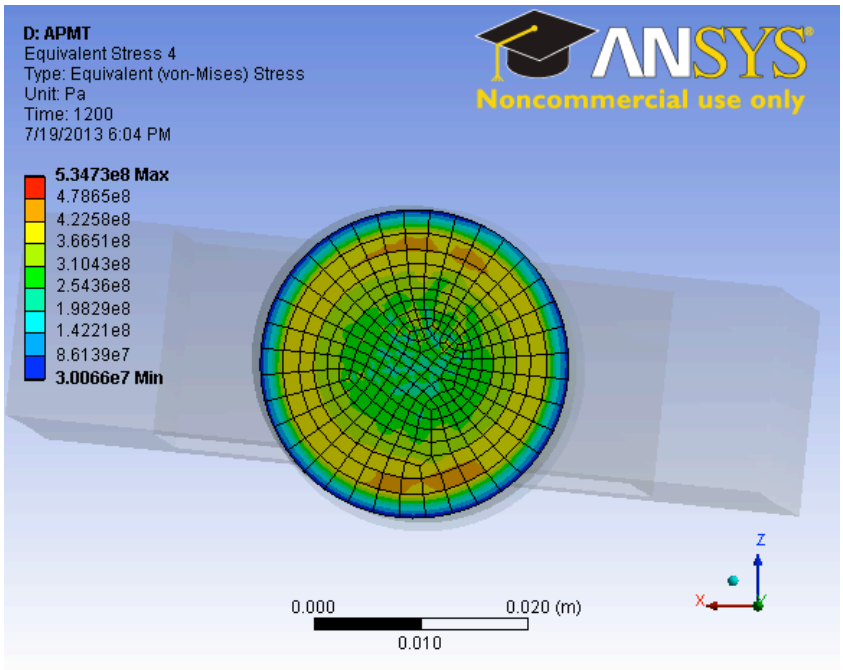

Figure 32. von Mises Stress Distribution at the Bondface at 1200°C for Plate That is Stiffer Than the Supporting Material.

As a result of the similarities of the APMT model with previous work the current model can be determined to be an accurate representation of the bonding.

CHAPTER IV

CONCLUSION

The diffusion bonding and subsequent SEM and EDS analysis yielded the weight percent data necessary to calculate the diffusion coefficients of zinc in the different materials under the different bonding conditions. The coefficients of thermal expansion of the bonding materials were experimentally found using a TMA. That data, along with other material properties found in literature, served as input values for a finite element model of the bonding process. A finite element model was created for each of the bonding situations and the stress distribution results were validated by comparison against previous research and analytical estimates. The results from the current work will aid in future study aimed at the design of fixtures to aid in the production of turbine components with complex geometries that have a spallation resistant layer diffusion-bonded over the top of core material with a higher creep strength.

Summary

The first portion of this research focused on the creation of diffusion-bonded samples of three different super alloys and the determination of the diffusion coefficient of the zinc interlayer used to bond the materials together. To achieve this, samples of each of the three materials: APMT, CM247LC, and

Rene 80, were bonded to themselves at varying times and temperatures. Each sample's bondface was ground to a surface roughness of approximately Ra=0.8 micron. Then the sample was extensively cleaned before being placed in the furnace. Samples were then sealed in the tube furnace flooded with commercially pure argon. Samples were created at times of 1, 3, 5, 10, and 20 hours at 1214°C, for 3 and 20 hours at 1155°C, and 30 minutes at 700°C. The bonded samples were then sectioned and analyzed with SEM and EDS to determine the weight percent of the diffusing zinc interlayer in areas moving away from the bond. Next, using the equation for the diffusion of a thin film into a semi-infinite sink, the diffusion coefficients were determined for each of the materials for every time and temperature tested.

The other portion of this research centered on the creating of a finite element model that accurately predicts the stresses present during the bonding process. The model was created using ANSYS Workbench 14.0. For the material constants of the model, the thermal expansion coefficients were determined for each material experimentally with a TMA; the remaining material properties were taken from literature. The analysis of the stresses caused by the thermal expansion of the materials was done in 12 steps. Each step calculated the stress at the bondface every one hundred degrees between room temperature and 1200°C. The stresses present during the heating and bonding of the samples for each of the three materials were analyzed. The stress distributions were then cross-referenced with similar finite element models from previous studies that also modeled the stress distributions during the bonding process. The cause for

the distribution of the stress was investigated. Then by comparing the results from the current finite element model to the results from previous studies it can be determined if the current model is a valid representation of the bonding.

Results Summary

In the first part of the study, the diffusion coefficient for the zinc interlayer diffusing into the parent material was calculated for each of the time and temperature combinations. It was found that the for Rene 80 and APMT the diffusion coefficient started at a maximum under the shortest bonding time at the bonding temperature of 1214°C and decreased as the time at the bonding temperature increased as well as when the bonding temperature decreased. The diffusion coefficient of the zinc interlayer in APMT decreased from 299.8 μm^2/min at the center of the bond during the bonding at 1214°C for 1 hour to 112.6 μm^2/min at the center of the bond during the bonding at 1214°C for 5 hours before the diffusion coefficient could no longer be determined at longer times at 1214°C. The diffusion coefficient at 1155°C reached only a maximum of 63.42 μm^2/min at the center of the bond during the bonding at 3 hours. Similarly, the diffusion coefficient of Rene 80 decreased from a maximum of 11.97 μm^2/min when bonded at 1214°C for 1 hour to a minimum of 3.18 μm^2/min at the center of the bond when bonded at 1214°C for 20 hours. The diffusion coefficient for the zinc in Rene 80 when bonded at 1155°C for 20 hours was 2.33 μm^2/min at the center of the bond. These numbers agree with literature that states that the diffusion coefficient decreases as time increases as well as when the

temperature decreases. The diffusion coefficients for the CM247LC, however, did not appear to follow any trend.

The diffusion coefficients for the nickel based alloys Rene 80 and CM247LC did approach a value that was theoretically determined for the diffusion of zinc in pure nickel. Additionally the approximate mass of zinc at the bond is greater at the center of the bond than at the edge of the bond supporting the evaporative metal bonding of the zinc. The diffusion coefficients of the zinc interlayer in the bonding materials will aid in the determination of a heating program for the creation of diffusion-bonded parts of more complicated geometries.

From the diffusion data samples it could be seen that the APMT created a bond between 5 and 10 hours at 1214°C where the zinc interlayer has diffused almost completely out of the parent material. However, after a bonding time of 20 hours at 1214°C the CM247LC and the Rene 80 still had zinc present in the joint and it was still diffusing. Therefore, a complete bond of the CM247LC and Rene 80 will take longer than 20 hours at 1214°C with a zinc interlayer and minimal preloading.

In the second portion of the study, the stresses present at the bondface during the temperature cycle were determined using finite element analysis in ANSYS Workbench 14.0. The stress distribution for the models where Rene 80 is bonding to itself and CM247LC is bonding to itself showed that for the situation in which the samples being bonded are the same material the stress is the greatest at the center of the bonding area decreasing out to the edge of the bond. The

stress decreases sharply at first and becomes more gradual and almost level towards the edge of the bond. This profile agrees with previous work that measured the hardness of the bondline as the hardness of the bond can be correlated to the pressure at which the bond was under when it formed. For the model where APMT is being bonded to itself with Rene 80 used as a buffer material to hold the sample in place, the stress distribution looks quite different. The stress across the middle of the bond region is relatively constant then increases to a maximum then decreases again before the edge of the bond where it is at a minimum. This stress distribution in the new model agrees with the stress distribution present in previous study where Al_2O_3–TiC was sandwiched around W18Cr4V. This agreement between the current finite element models and the stress distributions reported in previous research shows that the current models are correct representations of the real bonding process. It was also observed that the maximum stress at the bondface exceeded the yield stress of APMT. Therefore it can be assumed that the APMT would yield during diffusion. This yielding may in part contribute to the high diffusion coefficients of the zinc in the APMT. It was also determined that the contact between the jig and the hemispheres should be circular for an even stress distribution. The verification of the current finite element models serves as a starting point for further study into the design of a fixture for diffusion bonding of complex geometries.

Future Work

Future work with these specific superalloys may include the creation and analysis of diffusion-bonded samples where the APMT plate is bonded to Rene 80 and also to CM247LC. This analysis is important because the large difference of diffusion coefficients between the APMT and the Rene 80 as well as the CM247LC. In the bonding of materials with large differences in diffusion coefficients is when Kirkendall voids form. These can be mitigated somewhat by bonding the materials for the appropriate time and cooling them before the voids form. For that reason time at bonding analysis needs to be performed on these bonding situations to avoid the creation of voids. Studying this will determine the optimal bonding time for the creation of these joints.

Other future work includes the design of a jig for the bonding of turbine components that have Rene 80 or CM247LC as a core and APMT plate diffusion bonded over the top. The design of the jig can be made in a similar manner to that of the current finite element model and comparing the stress distribution to the current model. Contact between the hemispheres used to hold the materials for optimal contact should have a circular contact to ensure even stress distribution. The new design of the jig can then be made and tested in the actual bonding of multi layer turbine components. Testing of the fixture is necessary so that it can be confirmed that the zinc diffuses in the same manner when the part to be bonded has a much larger bonding area.

Conclusion

The study of the diffusion-bonding of Rene 80, CM247LC, and APMT is important in the creation of layered turbine components. These components are to be made with a core of Rene 80 or CM247LC, which have high creep strength, and plated with APMT, which has high TBC spallation resistance. By determining the diffusion coefficient of the zinc interlayer in the test materials, the heating schedule of larger and more complex bonded parts can be determined. The creation of a finite element model of the bonding process will also aid in the production of more complex parts. Simple models of the bonding setup and the determination of the stresses present at the bondface during bonding will aid in the design of a jig to bond more complex geometries.

APPENDIX

Appendix

EDS Diffusion Data and Calculated Diffusion Coefficients

APMT 700°C 30 min Center

Distance from Center x (μm)	Weight percent zinc (wt%)	x^2	Ln wt%
15	16.138	56.25	2.7812
30	3.941	506.25	1.3714
45	0.5	1406.25	-0.6931
60	0.349	2756.25	-1.0527
		m (1/ μm^2)	-1.38E-03
		D (μm^2/min)	6.0386
		R^2	0.83

APMT 700°C 30 min End

Distance from Center x (μm)	Weight percent zinc (wt%)	x^2	Ln wt%
15	10.338	56.25	2.3358
30	3.26	506.25	1.1817
45	0.632	1406.25	-0.4589
		m (1/ μm^2)	-2.03E-03
		D (μm^2/min)	4.0954
		R^2	0.9919

APMT 1155°C 3h Center

Distance from Center x (μm)	Weight percent zinc (wt%)	x^2	Ln wt%
10	0.72	25	-0.3285
20	1.076	225	0.0733
30	1.249	625	0.2223
40	1.587	1225	0.4618
50	1.406	2025	0.3407
60	1.34	3025	0.2927
70	1.335	4225	0.2889
80	1.74	5625	0.5539
90	1.482	7225	0.3934
100	1.568	9025	0.4498
110	1.234	11025	0.2103
120	1.131	13225	0.1231
130	1.017	15625	0.0169
140	1.146	18225	0.1363

150	1.155	21025	0.1441
160	1.159	24025	0.1476
170	1.021	27225	0.0208
180	0.867	30625	-0.1427
190	0.571	34225	-0.5604
200	0.62	38025	-0.4780
210	0.498	42025	-0.6972
220	0.527	46225	-0.6406
230	0.529	50625	-0.6368
240	0.488	55225	-0.7174
250	0.425	60025	-0.8557
		m (1/ μm^2)	-1.98E-05
		D (μm^2/min)	70.146
		R^2	0.7575

APMT 1155°C 3h End

Distance from Center x (μm)	Weight percent zinc (wt%)	x^2	Ln wt%
10	0.177	25	-1.7316
20	0.163	225	-1.8140
30	0.17	625	-1.7720
		m (1/ μm^2)	-
		D (μm^2/min)	-
		R^2	-

APMT 1155°C 20h Center

Distance from Center x (μm)	Weight percent zinc (wt%)	x^2	Ln wt%
50	0.525	625	-0.6444
100	0.536	5625	-0.6236
150	0.409	15625	-0.8940
200	0.457	30625	-0.7831
		m (1/ μm^2)	-
		D (μm^2/min)	-
		R^2	0.4063

APMT 1155°C 20h End

Distance from Center x (μm)	Weight percent zinc (wt%)	x^2	Ln wt%
50	0.187	625	-1.6766
100	0.341	5625	-1.0759
150	0.461	15625	-0.7744
		m (1/ μm^2)	-
		D (μm^2/min)	-
		R^2	-

APMT 1214°C 1h Cneter

Distance from	Weight percent	x^2	Ln wt%

Center x (μm)	zinc (wt%)		
75	2.588	1406.25	0.9509
150	1.941	12656.25	0.6632
225	0.688	35156.25	-0.3740
300	0.461	68906.25	-0.7744
375	0.35	113906.25	-1.0498
450	0.221	170156.25	-1.5096
		m (1/ μm^2)	-1.39E-05
		D (μm^2/min)	299.76
		R^2	0.8582

APMT 1214°C 1h End

Distance from Center x (μm)	Weight percent zinc (wt%)	x^2	Ln wt%
75	2.306	1406.25	0.8355
150	1.937	12656.25	0.6611
225	0.887	35156.25	-0.1199
300	0.293	68906.25	-1.2276
375	0.246	113906.25	-1.4024
		m (1/ μm^2)	-2.17E-05
		D (μm^2/min)	192.012
		R^2	0.9086

APMT 1214°C 3h Center

Distance from Center x (μm)	Weight percent zinc (wt%)	x^2	Ln wt%
50	0.397	625	-0.9238
100	0.188	5625	-1.6713
150	0.284	15625	-1.2588
		m (1/ μm^2)	-
		D (μm^2/min)	-
		R^2	-

APMT 1214°C 3h End

Distance from Center x (μm)	Weight percent zinc (wt%)	x^2	Ln wt%
50	0.19	625	-1.6607
100	0.214	5625	-1.5418
150	0.324	15625	-1.1270
		m (1/ μm^2)	-
		D (μm^2/min)	-
		R^2	-

APMT 1214°C 5h Center

Distance from Center x (μm)	Weight percent zinc (wt%)	x^2	Ln wt%
75	1.877	1406.25	0.6297
150	2.017	12656.25	0.7016

225	1.558	35156.25	0.4434
300	0.937	68906.25	-0.0651
375	0.67	113906.25	-0.4005
450	0.65	170156.25	-0.4308
		m (1/ μm^2)	-7.40E-06
		D (μm^2/min)	112.61
		R^2	0.8923

APMT 1214°C 5h End

Distance from Center x (μm)	Weight percent zinc (wt%)	x^2	Ln wt%
75	0.628	1406.25	-0.4652
150	0.394	12656.25	-0.9314
225	0.479	35156.25	-0.7361
		m (1/ μm^2)	-5.60E-06
		D (μm^2/min)	148.81
		R^2	0.1712

APMT 1214°C 10h Center

Distance from Center x (μm)	Weight percent zinc (wt%)	x^2	Ln wt%
75	0.398	1406.25	-0.9213
150	0.349	12656.25	-1.0527
225	0.538	35156.25	-0.6199
300	0.589	68906.25	-0.5293
375	0.497	113906.25	-0.6992
450	0.411	170156.25	-0.8892
		m (1/ μm^2)	-
		D (μm^2/min)	-
		R^2	0.0339

APMT 1214°C 10h End

Distance from Center x (μm)	Weight percent zinc (wt%)	x^2	Ln wt%
75	0.381	1406.25	-0.9650
150	0.434	12656.25	-0.8347
225	0.492	35156.25	-0.7093
		m (1/ μm^2)	-
		D (μm^2/min)	-
		R^2	-

APMT 1214°C 20h Center

Distance from Center x (μm)	Weight percent zinc (wt%)	x^2	Ln wt%
75	0.316	1406.25	-1.1520
150	0.223	12656.25	-1.5006
225	0.317	35156.25	-1.1489
		m (1/ μm^2)	-

		D (μm^2/min)	-
		R^2	-

APMT 1214°C 20h End

Distance from Center x (μm)	Weight percent zinc (wt%)	x^2	Ln wt%
75	0.245	1406.25	-1.4065
150	0.154	12656.25	-1.8708
225	0.209	35156.25	-1.5654
		m (1/ μm^2)	-
		D (μm^2/min)	-
		R^2	-

CM247LC 700°C 30 min Center

Distance from Center x (μm)	Weight percent zinc (wt%)	x^2	Ln wt%
10	16.721	25	2.8167
20	0.254	225	-1.3704
30	0.165	625	-1.8018
		m (1/ μm^2)	-6.75E-03
		D (μm^2/min)	1.2342
		R^2	0.6537

CM247LC 700°C 30 min End

Distance from Center x (μm)	Weight percent zinc (wt%)	x^2	Ln wt%
10	17.674	25	2.8721
20	7.021	225	1.9489
30	0.082	625	-2.5010
		m (1/ μm^2)	-2.03E-03
		D (μm^2/min)	4.0954
		R^2	0.9919

CM247LC 1155°C 3h Center

Distance from Center x (μm)	Weight percent zinc (wt%)	x^2	Ln wt%
10	7.583	25	2.0259
20	14.059	225	2.6433
30	9.778	625	2.2801
40	9.055	1225	2.2033
50	6.777	2025	1.9135
60	4.122	3025	1.4163
70	1.38	4225	0.3221
80	0.233	5625	-1.4567
90	0.033	7225	-3.4112
		m (1/ μm^2)	-7.72E-04
		D (μm^2/min)	1.7984
		R^2	0.9153

CM247LC 1155°C 3h End

Distance from Center x (μm)	Weight percent zinc (wt%)	x^2	Ln wt%
10	0	25	-
20	0.026	225	-3.6497
30	0	625	-
		m (1/ μm^2)	-
		D (μm^2/min)	-
		R^2	-

CM247LC 1155°C 20h Center

Distance from Center x (μm)	Weight percent zinc (wt%)	x^2	Ln wt%
10	0.111	25	-2.1982
20	0.017	225	-4.0745
30	0.05	625	-2.9957
		m (1/ μm^2)	-
		D (μm^2/min)	-
		R^2	-

CM247LC 1155°C 20h End

Distance from Center x (μm)	Weight percent zinc (wt%)	x^2	Ln wt%
10	0.126	25	-2.0715
20	0	225	-
30	0.11	625	-2.2073
		m (1/ μm^2)	-
		D (μm^2/min)	-
		R^2	-

CM247LC 1214°C 1h Center

Distance from Center x (μm)	Weight percent zinc (wt%)	x^2	Ln wt%
10	6.859	25	1.9256
20	5.589	225	1.7208
30	4.901	625	1.5894
40	2.403	1225	0.8767
50	1.487	2025	0.3968
60	0.29	3025	-1.2379
70	0.062	4225	-2.7806
		m (1/ μm^2)	-1.12E-03
		D (μm^2/min)	3.7369
		R^2	0.9784

CM247LC 1214°C 1h End

Distance from Center x (μm)	Weight percent zinc (wt%)	x^2	Ln wt%

10	4.397	25	1.4809
20	4.277	225	1.4533
30	3.761	625	1.3247
40	3.572	1225	1.2731
50	2.71	2025	0.9969
60	1.961	3025	0.6735
70	0.843	4225	-0.1708
80	0.493	5625	-0.7072
90	0.161	7225	-1.8264
		m (1/ μm^2)	-4.49E-04
		D (μm^2/min)	9.2840
		R^2	0.9688

CM247LC 1214°C 3h Center

Distance from Center x (μm)	Weight percent zinc (wt%)	x^2	Ln wt%
10	4.123	25	1.4166
20	3.959	225	1.3760
30	3.238	625	1.1750
40	3.482	1225	1.2476
50	2.766	2025	1.0174
60	2.805	3025	1.0314
70	1.766	4225	0.5687
80	1.661	5625	0.5074
90	1.25	7225	0.2231
100	0.857	9025	-0.1543
110	0.167	11025	-1.7898
120	0.168	13225	-1.7838
		m (1/ μm^2)	-2.43E-04
		D (μm^2/min)	5.7203
		R^2	0.9211

CM247LC 1214°C 3h End

Distance from Center x (μm)	Weight percent zinc (wt%)	x^2	Ln wt%
10	2.292	25	0.829424799
20	2.137	225	0.7594
30	1.808	625	0.5922
40	1.243	1225	0.2175
50	1.699	2025	0.5300
60	0.791	3025	-0.2345
70	0.844	4225	-0.1696
80	0.559	5625	-0.5816
90	0.095	7225	-2.3539
100	0.096	9025	-2.3434
		m (1/ μm^2)	-3.62E-04
		D (μm^2/min)	3.8346
		R^2	0.9111

CM247LC 1214°C 5h Center

Distance from Center x (μm)	Weight percent zinc (wt%)	x^2	Ln wt%
10	3.506	25	1.2545
20	3.381	225	1.2182
30	3.548	625	1.2664
40	3.262	1225	1.1823
50	2.518	2025	0.9235
60	2.644	3025	0.9723
70	2.236	4225	0.8047
80	1.824	5625	0.6010
90	1.247	7225	0.2207
100	0.898	9025	-0.1076
110	0.563	11025	-0.5745
120	0.666	13225	-0.4065
130	0.07	15625	-2.6593
140	0.04	18225	-3.2189
		m (1/ μm^2)	-2.25E-04
		D (μm^2/min)	3.7070
		R^2	0.8994

CM247LC 1214°C 5h End

Distance from Center x (μm)	Weight percent zinc (wt%)	x^2	Ln wt%
10	2.657	25	0.9772
20	1.774	225	0.5732
30	1.967	625	0.6765
40	1.189	1225	0.1731
50	1.168	2025	0.1553
60	1.285	3025	0.2508
70	0.838	4225	-0.1767
80	0.576	5625	-0.5516
90	0.375	7225	-0.9808
100	0.340	9025	-1.0788
110	0.165	11025	-1.8018
		m (1/ μm^2)	-2.22E-04
		D (μm^2/min)	3.7487
		R^2	0.9622

CM247LC 1214°C 10 Center

Distance from Center x (μm)	Weight percent zinc (wt%)	x^2	Ln wt%
10	3.67	25	1.3002
20	3.612	225	1.2843
30	3.543	625	1.2650
40	3.505	1225	1.2542
50	3.703	2025	1.3091

60	3.554	3025	1.2681
70	3.571	4225	1.2728
80	3.113	5625	1.1356
90	2.62	7225	0.9632
100	2.477	9025	0.9070
110	2.268	11025	0.8189
120	1.41	13225	0.3436
130	1.098	15625	0.0935
140	0.795	18225	-0.2294
150	0.49	21025	-0.7133
160	0.159	24025	-1.8389
		m (1/ μm^2)	-1.09E-04
		D (μm^2/min)	3.8191
		R^2	0.8887

CM247LC 1214°C 10 End

Distance from Center x (μm)	Weight percent zinc (wt%)	x^2	Ln wt%
10	0.079	25	-2.5383
20	0.136	225	-1.9951
30	0.217	625	-1.5279
		m (1/ μm^2)	-
		D (μm^2/min)	-
		R^2	-

CM247LC 1214°C 20h Center

Distance from Center x (μm)	Weight percent zinc (wt%)	x^2	Ln wt%
10	2.051	25	0.7183
20	2.194	225	0.7857
30	2.199	625	0.7880
40	2.036	1225	0.7110
50	1.998	2025	0.6921
60	2.354	3025	0.8561
70	0.751	4225	-0.2863
80	0.742	5625	-0.2984
90	0.192	7225	-1.6503
100	0.031	9025	-3.4738
		m (1/ μm^2)	-4.19E-04
		D (μm^2/min)	0.4975
		R^2	0.8414

CM247LC 1214°C 20h End

Distance from Center x (μm)	Weight percent zinc (wt%)	x^2	Ln wt%
10	0.123	25	-2.0956
20	0.136	225	-1.9951
30	0	625	-

		m (1/ μm^2)	-
		D (μm^2/min)	-
		R^2	-

Rene 80 1155°C 20h Center

Distance from Center x (μm)	Weight percent zinc (wt%)	x^2	Ln wt%
10	1.543	25	0.4337
20	4.215	225	1.4386
30	4.813	625	1.5713
40	4.544	1225	1.5138
50	3.85	2025	1.3481
60	4.431	3025	1.4886
70	2.96	4225	1.0852
80	3.459	5625	1.2410
90	3.003	7225	1.0996
100	2.871	9025	1.0547
110	2.22	11025	0.7975
120	1.874	13225	0.6281
130	1.775	15625	0.5738
140	0.763	18225	-0.2705
150	0.626	21025	-0.4684
160	0.301	24025	-1.2006
170	0.545	27225	-0.6070
180	0.243	30625	-1.4147
190	0.358	34225	-1.0272
		m (1/ μm^2)	-8.43E-05
		D (μm^2/min)	2.4713
		R^2	0.8615

Rene 80 1155°C 20h End

Distance from Center x (μm)	Weight percent zinc (wt%)	x^2	Ln wt%
10	0.218	25	-1.5233
20	0.106	225	-2.2443
30	0.281	625	-1.2694
		m (1/ μm^2)	-
		D (μm^2/min)	-
		R^2	-

Rene 80 1214°C 1h Center

Distance from Center x (μm)	Weight percent zinc (wt%)	x^2	Ln wt%
10	8.124	25	2.0948
20	7.934	225	2.0712
30	7.374	625	1.9980
40	7.163	1225	1.9689
50	5.636	2025	1.7292

60	4.356	3025	1.4716
70	2.791	4225	1.0264
80	1.99	5625	0.6881
90	1.25	7225	0.2231
100	0.384	9025	-0.9571
110	0.155	11025	-1.8643
		m (1/ μm^2)	-3.48E-04
		D (μm^2/min)	11.973
		R^2	0.9668

Rene 80 1214°C 1h End

Distance from Center x (μm)	Weight percent zinc (wt%)	x^2	Ln wt%
10	8.422	25	2.1308
20	7.333	225	1.9924
30	5.914	625	1.7773
40	4.182	1225	1.4308
50	3.316	2025	1.1988
60	2.153	3025	0.7669
70	0.909	4225	-0.0954
80	0.49	5625	-0.7133
90	0.313	7225	-1.1616
100	0.105	9025	-2.2538
		m (1/ μm^2)	-4.49E-04
		D (μm^2/min)	9.2840
		R^2	0.9688

Rene 80 1214°C 3h Center

Distance from Center x (μm)	Weight percent zinc (wt%)	x^2	Ln wt%
10	6.789	25	1.9153
20	6.972	225	1.9419
30	6.214	625	1.8268
40	5.591	1225	1.7212
50	5.328	2025	1.6730
60	4.709	3025	1.5495
70	4.144	4225	1.4217
80	3.398	5625	1.2232
90	2.699	7225	0.9929
100	2.081	9025	0.7328
110	1.242	11025	0.2167
120	0.626	13225	-0.4684
130	0.576	15625	-0.5516
140	0.467	18225	-0.7614
150	0.193	21025	-1.6451
160	0.167	24025	-1.7898
		m (1/ μm^2)	-1.62E-04
		D (μm^2/min)	8.5523

		R^2	0.9869

Rene 80 1214°C 3h End

Distance from Center x (μm)	Weight percent zinc (wt%)	x^2	Ln wt%
10	6.557	25	1.8805
20	6.256	225	1.8335
30	5.626	625	1.7274
40	5.618	1225	1.7260
50	5.506	2025	1.7058
60	4.589	3025	1.5237
70	4.02	4225	1.3913
80	2.936	5625	1.0770
90	2.794	7225	1.0275
100	1.628	9025	0.4874
110	1.004	11025	0.0040
120	0.795	13225	-0.2294
130	0.675	15625	-0.3930
140	0.391	18225	-0.9390
150	0.361	21025	-1.0189
		m (1/ μm^2)	-1.50E-04
		D (μm^2/min)	9.2654
		R^2	0.9834

Rene 80 1214°C 5h Center

Distance from Center x (μm)	Weight percent zinc (wt%)	x^2	Ln wt%
10	4.75	25	1.5581
20	3.575	225	1.2740
30	3.702	625	1.3089
40	3.762	1225	1.3250
50	3.437	2025	1.2346
60	3.318	3025	1.1994
70	2.995	4225	1.0969
80	3.504	5625	1.2539
90	2.592	7225	0.9524
100	1.743	9025	0.5556
110	1.142	11025	0.1328
120	1.131	13225	0.1231
130	0.876	15625	-0.1324
140	0.413	18225	-0.8843
150	0.252	21025	-1.3783
		m (1/ μm^2)	-1.25E-04
		D (μm^2/min)	6.6881
		R^2	0.9448

Rene 80 1214°C 5h End

Distance from	Weight percent	x^2	Ln wt%

Center x (μm)	zinc (wt%)		
10	3.046	25	1.1138
20	3.758	225	1.3239
30	3.558	625	1.2692
40	3.449	1225	1.2381
50	2.735	2025	1.0061
60	2.24	3025	0.8065
70	2.246	4225	0.8092
80	1.549	5625	0.4376
90	1.526	7225	0.4226
100	1.028	9025	0.0276
110	1.115	11025	0.1089
120	0.966	13225	-0.0346
130	0.558	15625	-0.5834
140	0.241	18225	-1.4230
150	0.102	21025	-2.2828
		m (1/ μm^2)	-1.46E-04
		D (μm^2/min)	5.7195
		R^2	0.9358

Rene 80 1214°C 10h Center

Distance from Center x (μm)	Weight percent zinc (wt%)	x^2	Ln wt%
10	2.66	25	0.9783
20	2.265	225	0.8176
30	2.207	625	0.7916
40	1.802	1225	0.5889
50	1.814	2025	0.5955
60	1.769	3025	0.5704
70	1.33	4225	0.2852
80	0.87	5625	-0.1393
90	1.029	7225	0.0286
100	0.944	9025	-0.0576
110	0.457	11025	-0.7831
120	0.313	13225	-1.1616
		m (1/ μm^2)	-1.20E-04
		D (μm^2/min)	3.4722
		R^2	0.9437

Rene 80 1214°C 10h End

Distance from Center x (μm)	Weight percent zinc (wt%)	x^2	Ln wt%
10	0.994	25	-0.0060
20	0.665	225	-0.4080
30	0.791	625	-0.2345
40	0.646	1225	-0.4370
50	0.415	2025	-0.8795
60	0.52	3025	-0.6539

70	0.454	4225	-0.7897
80	0.137	5625	-1.9878
		m (1/ μm^2)	-2.66E-04
		D (μm^2/min)	1.5694
		R^2	0.7901

Rene 80 1214°C 20h Center

Distance from Center x (μm)	Weight percent zinc (wt%)	x^2	Ln wt%
10	1.436	25	0.3619
20	1.668	225	0.5116
30	1.564	625	0.4472
40	1.832	1225	0.6054
50	1.518	2025	0.4174
60	1.495	3025	0.4021
70	1.405	4225	0.3400
80	1.23	5625	0.2070
90	1.489	7225	0.3981
100	1.088	9025	0.0843
110	1.139	11025	0.1302
120	1.058	13225	0.0564
130	0.629	15625	-0.4636
140	0.764	18225	-0.2692
150	0.36	21025	-1.0217
160	0.756	24025	-0.2797
170	0.258	27225	-1.3548
180	0.15	30625	-1.8971
		m (1/ μm^2)	-6.54E-05
		D (μm^2/min)	3.1855
		R^2	0.8532

Rene 80 1214°C 20h End

Distance from Center x (μm)	Weight percent zinc (wt%)	x^2	Ln wt%
10	0.903	25	-0.1020
20	0.692	225	-0.3682
30	1.047	625	0.0459
40	0.942	1225	-0.0598
50	1.071	2025	0.0686
60	1.031	3025	0.0305
70	0.96	4225	-0.0408
80	0.928	5625	-0.0747
90	0.68	7225	-0.3857
100	0.471	9025	-0.7529
110	0.466	11025	-0.7636
		m (1/ μm^2)	-6.23E-04
		D (μm^2/min)	0.3344
		R^2	0.5852

REFERENCES

[1] Williams, Robert H. Bunn, Matthew. Consonni, Stefano. Gunter, William. Holloway, Sam. Moore, Robert. Simbeck, Dale. “Advanced Energy Supply Techniques.” *World Energy Assessment: Energy and the Challenge of Sustainability*. Ed. Communications Development Incorporated. New York: United Nations Development Programme. 2000. 273-379. Print.

[2] Lee, Kang N. “Protective Coatings for Gas Turbines.” *The Gas Turbine Handbook*. U.S. Dept. of Energy-National Energy Technology Laboratory 4.4.2. 2006. 21 May 2013. Web.

[3] Viteri, Fermin. “Turbine-Based Zero Emmissions Plants.” *The Gas Turbine Handbook*. U.S. Dept. of Energy-National Energy Technology Laboratory 1.3.1.2. 2006. 21 May 2013. Web.

[4] Tamarin, Y. *Protective Coatings for Turbine Blades.* Materials Park: ASM International. 2006. Print.

[5] “Diffusion.” *Umm Al-Qura University.* UQU.edu.sa. Web. 20 May 2013. <http://uqu.edu.sa/files2/tiny_mce/plugins/filemanager/files/4300270/1/2/3/4/4.%20Diffusion.pdf>

[6] Callister, William D. Rethwisch *Fundamentals of Materials Science and Engineering: An Integrated Approach, 4th Edition.* New York. Wiley. May 2012. Print

[7] Garrett, B.R. Blank, G.F. Ranadive A.J. “Broad Applications of Diffusion Bonding.” Springfield. Clearinghouse for Federal Scientific and Technical Information. March 1966. Print.

[8] Cole, Frederic W. “Method of Diffusion Bonding” Patent 3789498. February 5, 1974.

[9] Orhan, N. Aksoy, M. Eroglu, M. “A new model for diffusion bonding and its application to duplex alloys.” *Materials Science and Engineering A*271 (1999) 458–468. Print.

[10] Thirunavukkarasu, V. Maniraj, J. Kumaresan, K. Senthil Kumar, K.M. Kanthavel, K. “Investigation and Experimental Analysis of Diffusion Bondingof AL 6061/Sicp Materials.” *International Journal for Manufacturing Science & Production.* Vol. 10, Nos 3-4, (2009). 213-229. Print.

[11] Maity, Joydeep. Pal, Tapan Kumar. Maiti, Rabindranath. “Transient liquid phase diffusion bonding of 6061-13 vol.% SiCp composite using Cu powder interlayer: mechanism and interface characterization.” *Journal of Material Science* (2010) Vol 45: 3575–3587. Print.

[12] Hurley, John P. Cavalli, Matthew N. 2011. *Preparation and Testing of Corrosion- and Spallation-Resistant Coatings.* University Turbine Systems Research Workshop. Columbus, Ohio.

[13] Chandler, Harry. *Metallurgy for the Non-Metallurgist.* Materials Park. ASM International. 1998. Print.

[14] Saha, Ratan Kumar. Khan, Tahir I. “Effect of bonding variables on TLP bonding of oxide dispersion strengthened superalloy.” *Journal of Material Science.* (2007) Vol 42: 9187–9193. Print.

[15] Li, Hong. Li, Zhuo-Xin. “Transient Liquid Phase Diffusion Bonding of Steel Sandwich Panels under Small Plastic Deformation: Lab Experiment, Modeling, and Application.” *Journal of Sandwich Structures and Materials* (2008) Vol 10: 247-266. Print.

[16] Lee, K.S. Huh, H. “Simulation of superplastic forming/diffusion bonding with finite-element analysis using the convective coordinate system.” *Journal of Materials Processing Technology* (1999) Vol. 89-90: 92-98. Print.

[17] Guoge, Zhang. Chandel, R.S. “Solid state diffusion bonding of Incoloy MA 956 to itself.” *Journal of Materials Science Letters* (2003) Vol 22: 1693–1695. Print.

[18] Liu, Jiakun. Cao, Jian. Lin, Xingtao. Song, Xiaoguo. Feng, Jicai. “Microstructure and mechanical properties of diffusion bonded single crystal to polycrystalline Ni-based superalloys joint.” *Materials and Design* (2013) Vol 49: 622–626. Print.

[19] Liua, J.D. Jina, T. Zhaoa, N.R. Wanga, Z.H. Suna, X.F. Guana, H.R. Hu, Z.Q. “Effect of transient liquid phase (TLP) bonding on the ductility of a Ni-base single crystal superalloy in a stress rupture test.” *Materials Characterization* (2008) Vol 59: 68–73. Print.

[20] Ekrami, A. Moeinifar, S. Kokabi, A.H. “Effect of transient liquid phase diffusion bonding on microstructure and properties of a nickel base superalloy Rene 80.” *Materials Science and Engineering A* (2007) Vol 456: 93–98. Print.

[21] Kim, I.S. Choi, B.G. Seo, S.M. Kim, D.H. Jo, C.Y. “Influence of heat treatment on microstructure and tensile properties of conventionally cast and directionally solidified superalloy CM247LC.” *Materials Letters* (2008) Vol 62: 1110–1113. Print.

[22] Safari, J. Nategh, S. “On the heat treatment of Rene-80 nickel-base superalloy.” *Journal of Materials Processing Technology* (2006) Vol 176: 240–250. Print.

[23] Guoge, Zhang. Chandel, R. S. Seow, H. P. “Solid-State Diffusion Bonding of Inconel Alloy 718 to 17-4 PH Stainless Steel.” *Materials and Manufacturing Processes* (2001) Vol 16 No 2: 265–279. Print.

[24] Pollock, Tresa M. Tin, Sammy. “Nickel-Based Superalloys for Advanced Turbine Engines: Chemistry, Microstructure, and Properties.” *Journal of Propulsion and Power* (2006) Vol. 22, No. 2, March–April: 361-374. Print.

[25] Chen, S.D. Soh, A.K. Ke, F.J. “Molecular dynamics modeling of diffusion bonding.” *Scripta Materialia* (2005) Vol 52: 1135–1140. Print.

[26] Assadi, H. Shirzadi, A.A. Wallach, E.R. “Transient Liquid Phase Diffusion Bonding Under a Temperature Gradient: Modeling of the Interface Morphology.” *Acta Materialia* (2001) Vol 49: 31–39. Print.

[27] Bano, Nafisa. Nganbe, Michel. “Modeling of Thermal Expansion Coefficients of Ni-Based Superalloys Using Artificial Neural Network.” *Journal of Materials Engineering and Performance* (2013) Vol 22: 952–957. Print.

[28] Luo, Xian. Yang, Yanqing. Li, Jiankang. Yuan, Meini. Huang, Bin. Chen, Yan. “An analysis of thermal residual stresses in SiC_f/Cu composites when TiC or Ni as binder.” *Materials and Design* (2008) Vol 29: 1755–1761. Print.

[29] Feng, J. Wang, D. Liu H. Li, Z. “Finite element simulation of thermal stress during diffusion bonding of Al_2O_3 ceramic to aluminium.” *IoM Communications Ltd. Published by Maney for the Institute of Materials, Minerals and Mining.* (2002). Print.

[30] Raevska, Snejana. “Reduction of the stresses introduced during the diffusion bonding of dissimilar materials.” *Journal of Materials Processing Technology* (1998) Vol 77: 50–53. Print.

[31] Travessa, Dilermando. Ferrante, Maurizio. den Ouden, Gert. “Diffusion bonding of aluminium oxide to stainless steel using stress relief interlayers.” *Materials Science and Engineering* A (2002) Vol 337: 287-296. Print.

[32] Xiaoqin, Shen. Yajiang, Li. Putchkov, U.A. Juan, Wang. Wanqun, Huang. “Finite-element analysis of residual stresses in Al_2O_3–TiC/W18Cr4V diffusion bonded joints.” *Computational Materials Science* (2009) Vol 45: 407–410. Print.

[33] Yang, Yanling. Peng, Liming. Fu, Penghuai. Hu, Bin. Ding, Wenjiang. Yu, Baozheng. “Effects of Process Parameters on the Macrostructure of a Squeeze-Cast Mg-2.5 mass%Nd Alloy.” *Materials Transactions* (2009) Vol. 50, No. 12: 2820-2825. Print.

[34] “Nickel Based Equiax.” *C-M Group.* Specialty Materials and Alloys Group. 2004. Web. 22 September 2012. <http://www.cmgroup.com/ vacuum_melt_index/nickel_base_equiax.htm>

[35] “Kanthal APMT.” *Kanthal.* AB Sandvivik Materials Technology. 22 September 2012. Web.

[36] McNally, Dustin. *Modeling of Diffusional Bonding Using Thermodynamic Simulation Software.* Thesis, University of North Dakota. (2007)

[37] Itoh, Y. Saitoh, M. Takaki K. Fujiyama, K. “Effect of high-temperature protective coatings on fatigue lives of nickel-based superalloys.” *Fatigue & Fracture of Engineering Materials & Structures* (2001) Vol 24: 843–854. Print.

[38] Wada, K. Yan, L. Takahashi, M. Takaishi, K. Furukawa, T. “Degradation of gas turbine blade materials in integrated coal-gasification combined cycle plant.” *Materials at High Temperatures* (2001) Vol 18 No 2: 131–138. Print.

[39] Jonsson, Bo. Lu, Qin. Chandrasekaran, Dilip. Berglund, Roger. Rave, Fernando. “Oxidation and Creep Limited Lifetime of Kanthal APMT, a Dispersion Strengthened FeCrAlMo Alloy Designed for Strength and Oxidation Resistance at High Temperatures.“ *Oxidation of Metals* (2013) Vol 79: 29-39. Print.

[40] Budynas, Richard G. Nisbett, J. Keith. *Shingley’s Mechanical Engineering Design, 8th Edition.* New York. McGraw-Hill. 2008. Print.

[41] “Surface Finish Roughness Chart” *jvnw.com.* Web. July 8, 2013. <http://jvnw.com/images/components/finishes/JVNWFinishChart.pdf>

[42] Poirier, D.R. Geiger, G.H. *Transport Phenomena in Materials Processing.* Warrendale. The Minerals, Metals & Materials Society. 1994. Print.

[43] “Chapter 1, Fick’s Laws and Macroscopic Diffusion.” *jrgreer.caltech.edu.* J.R. Greer. Web. July 8, 2013. <http://jrgreer.caltech.edu/content/teaching/MS133Files/Notes/Lect1MS133JRG.pdf>

[44] Butrymowicz, D.B., et al. “Diffusion in Copper and Copper Alloys Part IV. Diffusion in Systems Involving Elements of Group VIII.” *J. Phys. Chem. Ref. Data*, (1976). Vol 5 No. 1: 103-200. Print.

[45] Zacherl, Chelsey L. *A Computational Investigation of the Effect of Alloying Elements on the Thermodynamic and Diffusion Propertiesof FCC Ni Alloys, With Application to the Creep Rate of Dilute Ni-X Alloys.* Thesis, Pennsylvania State University. (2012)

[46] “Molybdenum, Mo, Annealed.” *Matweb.* Matweb LLC. Web. 20 May 2013. <www.matweb.com/search/datasheet_print.aspx?matguid=ef57c33963404798ad0301a05692312a>

[47] “Rene 80.” *Stainless SS.* Jiangyou Longhai Special Steel Co, Ltd. Web. 20 May 2013. <www.steelss.com/High-alloy/rene-80.html>

[48] “AISI E 52100 Steel.” *Matweb.* Matweb LLC. Web. 20 May 2013. <www.matweb.com/search/datasheet_print.aspx?matguid=d0b0a51bff894778a97f5b72e7317d85>

[49] Sehitoglu, H. Maier, HJ. *Thermo-mechanical Fatigue Behavior of Materials: Third Volume*. Materials Park: ASM International. 2000. Print.

[50] Moore, Zachary. *Life Modeling of Notched CM247LC DS Nickel-Base Superalloy.* Thesis, Georgia Institute of Technology. (2008)

[51] Jichi, Florin G. *Theoretical and Experimental Investigation of Magnetostrictive Tagged Composite Beams*. Thesis, University of South Carolina. (2000)